Nonidentical-particle femtoscopy at $\sqrt{s_{NN}} = 200$ GeV in hydrodynamics with statistical hadronization

Adam Kisiel[1,2,*]

[1]*Department of Physics, Ohio State University, 1040 Physics Research Building, 191 West Woodruff Avenue, Columbus, Ohio 43210, USA*

[2]*Faculty of Physics, Warsaw University of Technology, PL-00661 Warsaw, Poland*

(Received 1 October 2009; published 21 June 2010)

Nonidentical-particle femtoscopy probes not only the size of the emitting system, but also the emission asymmetries between particles of different masses, which are intimately related to the collective behavior of matter. We apply the technique to simulations from the THERMINATOR + LHYQUID model of heavy-ion collisions at $\sqrt{s_{NN}} = 200$ GeV. We present predictions for all pairwise combinations of pions, kaons, and protons and discuss their interpretation. We show that kaon and proton distributions are strongly influenced by flow: the source gets smaller and shifted to the outside with growing p_T, while for pions the shift is significantly smaller, producing an emission asymmetry. We explain how particles coming from decays of hadronic resonances enhance the asymmetry signal coming from flow, contrary to naive expectations. Emphasis is put on extracting this unique information on the collective behavior of matter from nonidentical-particle correlations. We also present, in detail, the technical aspects of the nonidentical-particle femtoscopy technique applied to data from heavy-ion collisions. We list the sources of systematic errors coming from the method itself and the usual assumptions. We describe robust analysis methods and discuss their limitations.

DOI: 10.1103/PhysRevC.81.064906 PACS number(s): 25.75.Dw, 25.75.Ld

I. INTRODUCTION

Femtoscopy has been used for more than 35 years [1,2] to measure sizes of the systems created in nucleus-nucleus collisions. Initially it was developed for analyzing the two-particle correlations arising from wave-function symmetrization for pairs of identical particles [3] and was similar in mathematical framework to the "HBT (Hanbury Brown and Twiss) interferometry" used in astronomy [4–6]. Later it was realized that similar correlations arise owing to final-state interactions (FSIs; Coulomb and strong) between particles that are not necessarily identical [7–11].

Femtoscopy of nonidentical particles provides unique information: while identical-particle correlations usually only measure the "size" of the emitting region (more precisely, the second moments of the emission function), nonidentical correlations can, thanks to the very fact that they correlate particles that are not identical, also measure the relative emission shifts (the first moments of the emission function) [7–10,12–14].

The unique features of nonidentical-particle femtoscopy was used in low-energy nuclear collisions to study the time ordering of the emission of various nuclear fragments from the compound nucleus [15–19]. This required measuring time differences from several to hundreds of femtometers per c [16–19].

In this work we focus on the applications of this technique in collisions of ultra-relativistic heavy ions, specifically Au ions in the Relativistic Heavy Ion Collider (RHIC) at Brookhaven National Laboratory, although the discussion is also relevant for lower-energy [in the Super Proton Synchrotron (SPS) at CERN] and higher-energy (in the Large Hadron Collider at CERN) energy collisions.

One of the major discoveries at the RHIC has been the observation of quark-gluon plasma, which was found to behave collectively, very much like a fluid [20,21]. Hydrodynamic equations seemed to describe this behavior well in the momentum sector. However, attempts to simultaneously describe the space-time behavior measured by femtoscopy have not been successful until recently. This failure was commonly referred to as the "RHIC hydro-HBT puzzle" [22–25]. Through a detailed analysis of the experimental data and various improvements of the hydrodynamic description, it was realized that certain assumptions had to be modified to properly describe both sets of observables. The initial condition was changed to one that uses a Gaussian initial profile for the transverse energy density [26], which results in faster development of the initial flow, compared to the traditional one [27,28]. The equation of state used did not exhibit a first-order phase transition but, rather, a crossover. Detailed simulation of the resonance contribution in the later stage of the collisions was carried out [26]. In addition, some studies have suggested that the introduction of viscosity and universal (pre-equilibrium) flow into the model may also play an important role [29,30].

The hydrodynamic scenario produces specific space-momentum correlation patterns, which are commonly referred to as flow. The system created in the heavy-ion collision expands rapidly outward, showing a very strong radial flow, which is observed in the modification of the single-particle inclusive p_T spectral shape. In addition, in noncentral collisions, the initial overlap region has an elongated (usually described as "almond") shape, and this spatial asymmetry is converted to a momentum one in the final state. This momentum asymmetry is observed as an elliptic flow v_2 and is the subject of very intensive theoretical and experimental

*kisiel@if.pw.edu.pl

studies; see Refs. [31] and [32] for recent reviews. However, because of its origin, it is small in central collisions. This is unfortunate, as it is in central collisions that we expect to create the largest volume of deconfined matter, which we would like to study. Both the p_T spectra and the elliptic flow are observables depending only on the momenta of the particles, so their connection to space-time can only be indirectly inferred. To access it directly we employ femtoscopic techniques. It is argued that the fall of the "femtoscopic radii" with the particle's m_T can be interpreted as a decrease in the "lengths of homogeneity," a direct consequence of radial and longitudinal flow [33]. However, one might come up with alternative explanations, involving temperature gradients that produce similar dependencies [34]. In this work we show how the collective flow present in hydrodynamic and transport models, in addition to the effects just discussed, produces differences in average emission points between particles of different masses. We also describe how these emission asymmetries can be accessed via nonidentical-particle femtoscopy [35]. Measuring such effects would enable us to eliminate scenarios alternative to hydrodynamic expansion and provide a crucial and strict test for the models. Results on π^+-π^- and π-proton correlations have been reported previously by NA49 [35,36] and the CERES experiment [37,38] at the SPS. The first results on pion-kaon correlations have been reported by STAR [39]. Preliminary results on π-Ξ correlations from STAR have also been presented [40]. Proton-Λ correlations have also been measured by STAR [41], but that analysis did not attempt to extract emission asymmetries.

To properly simulate the emission asymmetries between particles of different masses, we need a model that has all the important features: a hydrodynamic phase, which produces space-momentum correlations, and an hadronic phase, where at least the hadronic resonance decays and propagation are treated. In addition, the model should provide the space-time freeze-out coordinates of particles, so that femtoscopic calculations can be carried out. It should, as much as possible, reproduce the available data on particle spectra and femtoscopy. Hydrodynamics-inspired "blast-wave" parametrization of freeze-out have been used to model asymmetries between nonidentical particles [42]. That study nicely illustrated the connection between strong collective matter behavior and asymmetries; however, it used simplified emission functions and neglected resonance propagation and decay. In this work we have chosen the THERMINATOR + LHYQUID model, which we introduce in Sec. II. In Sec. III we describe the particular set of simulations of heavy-ion collisions at six centralities that we have carried out. We calculated the system size and emission asymmetry for three pair types: pion-kaon, pion-proton, and kaon-proton. We discuss the origins of the asymmetry and provide the connection to the space-momentum correlations coming from flow. We also discuss other nonflow sources of emission asymmetries and provide a quantitative estimate of all contributions.

Having emphasized the importance of the emission asymmetries phenomenon, we describe the theoretical framework of nonidentical-particle correlations in Sec. IV. Then we move to the technical aspects of the measurement in heavy-ion collisions in Sec. V. We argue that a specific mathematical representation of nonidentical correlation functions [the spherical harmonics (SH) decomposition] shows remarkable synergies with the analysis and maximizes the statistical significance of the emission asymmetry signal. We describe the measurement procedure that enables recovery of the properties of the model emission function from the "experimental" correlation function. In Sec. VI we test the robustness of the procedure, list the assumptions and the approximations that must be employed, and estimate the systematic error coming from the technique itself. We show that the most important contribution to this error is the correct estimation of the fraction of non–femtoscopically correlated pairs (traditionally called the "purity"). We analyze this effect in detail and present purity estimates, based on our model of choice, which can be directly used in the experimental analysis.

Finally, in Sec. VII we use numerical simulations with the THERMINATOR model to produce "experimental-like" correlation functions, which we then analyze with the methods presented earlier. We demonstrate that the method is able to recover the theoretical input values. The results presented in this section are the theoretical predictions for the overall system size as well as the emission asymmetry for all considered pair types and six centralities. They can be immediately compared to the experimental results with a minimal number of approximations and, therefore, minimal systematic uncertainty.

II. LHYQUID + THERMINATOR MODEL

In this work we use what we call the *standard approach*, consisting of ideal-fluid hydrodynamics followed by statistical hadronization. Numerous calculations have been performed in this framework, with the common difficulty [22] of simultaneously describing femtoscopy and other signatures in the data. More precisely, the RHIC HBT puzzle [22–25] refers to problems in reconciling the large value of the elliptic flow coefficient v_2 with the identical-particle interferometry in calculations based on hydrodynamics [43–47]. Recently, a successful uniform description of soft observables at the RHIC has been accomplished, including the femtoscopic radii, within the standard approach [26]. The essential ingredients of this analysis were a Gaussian initial condition for hydrodynamics, an early start of the evolution, a state-of-the art equation of state with smooth crossover, and the use of THERMINATOR [48] with all resonances from SHARE [49] incorporated to carry out the statistical hadronization at the freeze-out surface temperature of 150 MeV. The interplay of these elements resulted in a simultaneous description of the transverse-momentum spectra of pions, kaons, and protons, the v_2, and the femtoscopic correlation radii of pions, including full centrality, k_T, and reaction plane dependence of azimuthally sensitive HBT signatures [50].

In this section we describe the essential elements of our method to the extent that they are necessary for the presented results. More details concerning the hydrodynamics are given in Refs. [26], [51], and [52], while the method used for femtoscopic calculations has been presented in Ref. [53].

A. Initial condition

As reported in Ref. [26], the use of the initial condition for hydrodynamics of the Gaussian form,

$$n(x, y) = \exp\left(-\frac{x^2}{2a^2} - \frac{y^2}{2b^2}\right), \tag{1}$$

where n is the initial energy density, while x and y denote the transverse coordinates, leads to a much better uniform description of the data for the p_T spectra, v_2, and pionic femtoscopic radii compared to the use of the standard initial condition from the Glauber model.

The width parameters a and b depend on centrality. To estimate realistic values for them we run the GLISSANDO [54] Glauber Monte Carlo simulations, which include eccentricity fluctuations [55,56]. Then we match a^2 and b^2 to reproduce the values $\langle x^2\rangle$ and $\langle y^2\rangle$ from the GLISSANDO profiles. Thus, by construction, the spatial RMS radius of the initial condition and its eccentricity are the same as those from the Glauber calculation. Nevertheless, the shape is not the same. The Gaussian profiles are sharper near the origin, which results in a faster buildup of the Hubble-like flow in the hydrodynamical stage.

The Glauber calculations, needed to obtain the a and b parameters, correspond to the mixed model [57], where the number of produced particles is proportional to $(1-\alpha)N_w/2 + \alpha N_{\rm bin}$, with N_w and $N_{\rm bin}$ denoting the number of wounded nucleons [58] and binary collisions, respectively. The parameter $\alpha = 0.145$ for the top RHIC energy [59,60]. The inelastic nucleon cross section is 42 mb for the RHIC [61]. The simulations incorporate the fluctuations of orientation of the fireball (the variable-axis geometry), which result in increased eccentricity compared to the fixed-axis geometry [62]. Finally, the expulsion distance of 0.4 fm is used in the generation of the nuclear distributions. A source-dispersion parameter of 0.7 fm is used. It describes the random displacement of the source from the center of the wounded nucleon or the binary-collision position [54].

The values of the a and b parameters for various centralities and the corresponding eccentricity parameters,

$$\epsilon^* = \frac{b^2 - a^2}{a^2 + b^2}, \tag{2}$$

are reported in Table I.

The energy-density profile, Eq. (1), determines the initial temperature profile via the equation of state [52]. The initial central temperature T_i is a parameter dependent on centrality. For RHIC calculations it is adjusted to reproduce the total particle multiplicity.

B. Hydrodynamics

The hydrodynamics equations used in this work are described in greater detail in Refs. [51] and [52]. We use inviscid (ideal-fluid), baryon-free, boost-invariant hydrodynamics. The equations are written in terms of the velocity of sound c_s, whose temperature dependence encodes the full information on the equation of state of the system. We incorporate the known features of $c_s(T)$, which, at high temperatures, are given by the lattice QCD calculations [63]; at a low T they follow from the hadron gas including all resonances, while at an intermediate T an interpolation is used. No sharp phase transition, but, rather, a smooth crossover, is built in, in accordance with the present knowledge of the thermodynamics of QCD at zero baryon chemical potential. The plot of the resulting $c_s(T)$ is given in Ref. [26].

The initial proper time of the start of hydrodynamics is fixed at the value

$$\tau_0 = 0.25 \text{ fm}. \tag{3}$$

This early start of hydrodynamics allows for a fast generation of transverse flow, similar to the effect described in Ref. [30].

C. Freeze-out

Hydrodynamic evolution proceeds until freeze-out occurs, where the assumed condition for the *universal* freeze-out temperature is $T_f = 150$ MeV. This value is somewhat lower than in several fits of the chemical freeze-out [64–66]; however, it agrees with the recently made global fits to particle transverse momentum spectra in Refs. [67] and [68], where a value of about 150 MeV was obtained for the kinetic freeze-out temperature.[1]

THERMINATOR is used to carry out statistical hadronization at the freeze-out hypersurface according to the Cooper-Frye formulation [69]. According to the assumed single-freeze-out approximation, identifying the kinetic and chemical freeze-out temperatures, rescattering processes after freeze-out are neglected. We have checked that the collision rate after freeze-out is moderate for the hypersurfaces applied in this work.

[1]The use of this lower freeze-out temperature requires the introduction of the strangeness inequilibrium factors γ_s to reproduce the abundances of strange particles [67].

TABLE I. Shape parameters a and b in Eq. (1) for various centrality classes obtained by matching $\langle x^2\rangle$ and $\langle y^2\rangle$ to GLISSANDO simulations, the variable-axis eccentricity ϵ^*, and the central temperature T_i.

	RHIC Au + Au at $\sqrt{s_{NN}} = 200$ GeV, at c (%)								
	0–5	5–10	10–20	20–30	30–40	40–50	50–60	60–70	70–80
a (fm)	2.70	2.54	2.38	2.00	1.77	1.58	1.40	1.22	1.04
b (fm)	2.93	2.85	2.74	2.59	2.45	2.31	2.16	2.02	1.85
ϵ^*	0.08	0.12	0.18	0.25	0.31	0.36	0.41	0.46	0.52
T_i (MeV)	500	491	476	460	429	390	344	303	261

We estimate it by considering a pion straight-line trajectory and counting the number of encounters with other particles closer than the distance corresponding to the pion-hadron cross section. The average number of these trajectory crossings is about 1.5–1.7 per pion. This shows that the single-freeze-out approximation [65] works reasonably well for the present case. At a more detailed level, one could use hadronic afterburners to model the elastic collisions [70–72] or attempt the hydrokinetic approach implemented in Refs. [27], [28], and [73].

D. Two-particle femtoscopy

The method used for femtoscopic analysis of the THERMINATOR model output was described in detail in Ref. [53]. The features of the formalism specific to nonidentical-particle correlations are described in Sec. IV. Their discussion is one of the main points of this work.

III. MODEL PREDICTIONS FOR THE RELATIVISTIC HEAVY ION COLLIDER

In this section we discuss the general trends that are expected to emerge in the nonidentical correlations. We also discuss their physical origins and the possible physics conclusions that can be drawn when they are observed experimentally. Later in this paper, we see how these trends manifest themselves in the calculations and we test whether it is indeed possible to observe them in the experiment.

Following convention, we assign the the symbol x for the emission points of single particles, usually used as a vector, $\boldsymbol{x}$, or as a vector magnitude, x. The momentum of a particle is denoted p. The single-particle velocity is β. We also define the pair variables. Relative separation between particles (vector) is $\boldsymbol{r} = \boldsymbol{x}_1 - \boldsymbol{x}_2$. We use the out-side-long coordinate system, where the *long* or longitudinal direction is along the beam axis, the *out* or outward direction is along the pair total transverse momentum, and the *side* or sideward direction is perpendicular to the other two. In a longitudinally comoving system (LCMS) the pair longitudinal momentum vanishes: $p_{1,\mathrm{long}} = -p_{2,\mathrm{long}}$. In the pair rest frame (PRF; also called the pair center of mass), the pair center of mass rests: $\boldsymbol{p}_1 = -\boldsymbol{p}_2$. In our convention all pair variables in PRF are marked with an asterisk. The pair relative half-momentum is denoted k^* and is equal to the *first* particle's momentum in the PRF. The pair total momentum is denoted P (or sometimes K, which is traditionally used in identical-particle femtoscopy). All single-particle coordinates as well as pair relative variables are designated by lowercase letters. In contrast, we use uppercase letters to denote the parameters of distributions. In particular, we call the variance or the two-particle separation distribution R. We call the mean of this distribution μ (with an L superscript if they are defined in an LCMS). We refer the reader to the Appendix for explicit mathematical formulas as well as relations between source characteristics in the two reference frames.

The discussion that follows is based on an example calculation from the THERMINATOR + LHYQUID model, done for parameters tuned to the central (0–5%) RHIC Au + Au collisions at $\sqrt{s_{NN}} = 200$ GeV. Whenever we mention RHIC Au + Au calculations we mean simulations at the top RHIC energy.

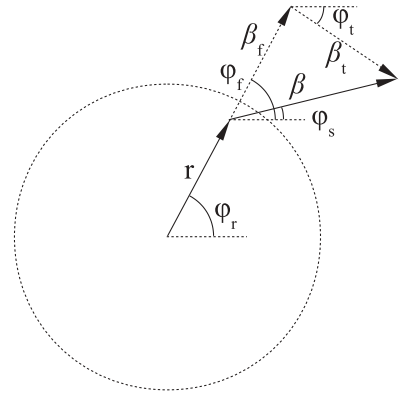

FIG. 1. Diagram of the particle's velocity β decomposition into the flow β_f and thermal β_t components.

A. Emission asymmetries

Hydrodynamic evolution of matter implies strong space-momentum correlations in particle emission. Particles emitted from a given fluid cell will have a velocity that is a combination of two components: the fluid cell velocity $\boldsymbol{\beta}_f$ [taken from the flow field $u_\mu(\boldsymbol{r})$] and the thermal velocity $\boldsymbol{\beta}_t$. This is shown schematically in Fig. 1.

The system created in a heavy-ion collision, when modeled in hydrodynamics, naturally develops a collective behavior—the radial flow in the transverse plane; that is, matter is collectively moving "outward" from the central axis of the source to the outside. In essence this is an x-p correlation: the direction ϕ_f of the fluid element's transverse velocity is aligned with its transverse position vector direction ϕ_r. When the fluid element emits particles, all of them will have the same common flow velocity β_f taken directly from u_μ. To this velocity one adds a thermal component β_t, which has a random direction ϕ_t in the rest frame of the fluid element. It will dilute the x-p directional correlation. Let us now consider the mean emission point of a single particle, more specifically its component parallel to the velocity [74]:

$$x_{\mathrm{out}} = \frac{\boldsymbol{x}\boldsymbol{\beta}}{\beta} = \frac{r(\beta_f + \beta_t \cos(\phi_t - \phi_f))}{\beta}. \tag{4}$$

We analyze its average over particles at a fixed β. If we assume a Gaussian density profile with radius r_0 and linear transverse velocity profile $\beta_f = \beta_0 r/r_0$, then we obtain [74]

$$\langle x_{\mathrm{out}} \rangle = \frac{\langle r\beta_f \rangle}{\left\langle \sqrt{\beta_t^2 + \beta_f^2} \right\rangle} = \frac{r_0\beta_0\beta}{\beta_0^2 + T/m_t}, \tag{5}$$

where we have explicitly given the formula for the velocity component coming from temperature. Pions and kaons emitted from the fluid element will have the same common flow velocity β_f (and different momenta). They will also get a random thermal kick, depending on the momentum. For a pion the same p_T kick will mean a much larger *velocity* β_t

kick than for a kaon. The final velocity direction of a pion will be, on average, less correlated with its emission position than that of a kaon. We assume that the spatial characteristics of pion and kaon emission are the same and the flow velocity is also the same. Hence, for both pions and kaons, $\langle r\beta_f \rangle$ is the same. The only difference is the T/m_T component, which is smaller for kaons. Therefore, $\langle x_{\text{out}} \rangle$ for pions is smaller than $\langle x_{\text{out}} \rangle$ for kaons. To summarize: when correlating pions and kaons with the same velocity (or more generally, two nonidentical particles of different masses, but the same velocity), pions (lighter particles) appear to be, on average, emitted closer to the center of the system than kaons (heavier particles). Consequently, hydrodynamics predicts a negative emission asymmetry $\mu_{\text{out}}^{\text{light,heavy}} = \langle r_{\text{out}}^{\text{light,heavy}} \rangle = \langle x_{\text{out}}^{\text{light}} - x_{\text{out}}^{\text{heavy}} \rangle$ between nonidentical particles of different masses.[2]

Let us discuss various limits in Eq. (5). When there is no flow ($\beta_f = 0$), all average emission points are 0 and the asymmetry vanishes. If the temperature is very high compared to the flow velocity (or more generally the random component dominates over the correlated one), the average emission point is 0 (center of the source). If this happens for both particles, the asymmetry is 0. If it happens for only one of them, the asymmetry exists. If the flow velocity strongly dominates over temperature, and particles are emitted from the same system, both average emission points are strongly shifted by the same amount, and consequence the asymmetry is again small. From the discussion we see that the existence of emission asymmetry is not trivial and only arises in a system where both random(thermal) and correlated(flow) velocities exist and are comparable in magnitude.

We illustrate the consequences that this mechanism has for the particle's emitting regions using the THERMINATOR calculations for central Au + Au collisions at the top RHIC energy as an example. First, we focus on the "primordial" particles, that is, particles coming directly from the hydrodynamical stage. Let us consider two variables:

$$x_{\text{out}} = \boldsymbol{x}\,\boldsymbol{p}_T/p_T, \qquad x_{\text{side}} = \boldsymbol{x} \times \boldsymbol{p}_T/p_T. \tag{6}$$

The first one is the component of the particle's transverse emission vector parallel to the particle's transverse momentum; the other is the perpendicular component. In Fig. 2(a) the distributions of these emission components are shown for primordial kaons. A strong correlation is seen: all particles moving "upward" (to the positive out direction) are emitted from the positive x_{out} part of the source. This focusing of the particle's emission has two distinct effects: the overall size of the emitting region shrinks in both the out and the side direction and the average emission position shifts in the out direction but not in the side direction. Looking at Fig. 3(a), one sees the same effects, but to a much smaller degree, for pions with the same velocity: the size is shrunk, but not as much, the average emission position is also shifted but by a smaller amount. The exact numerical values for the "size" (or variance) and "shift" (or mean) of these distributions are reported in Table II. Figure 4 shows analogous pictures for protons. As expected, the effect is the strongest there, as protons have almost twice the mass of kaons.

From the preceding discussion, and the numerical values in Tables II and III, one immediately sees that hydrodynamics produces two distinct trends in femtoscopic observables. (a) The size of the emitting system gets smaller with increasing p_T of the particle. This effect is well understood theoretically (the so-called "lengths of homogeneity") and universally observed experimentally in femtoscopy in heavy-ion collisions ("m_T scaling") [24]. (b) Average emission points of particles with different p_T values (e.g., with the same velocity but a different mass) are different, and this difference is well defined:

[2]We have chosen the convention of always taking the lighter particle to be first in the pair.

TABLE II. Single-particle source parameters (mean $\langle r \rangle$ and RMS X) for three particle types in selected kinematic regions.

Particle	β	p_T (GeV/c)	X_{out} (fm)	$\langle x_{\text{out}} \rangle$ (fm)	X_{side} (fm)	$\langle x_{\text{side}} \rangle$ (fm)
			Primordial particles			
K	0.6–0.8	0.42–0.56	2.68	4.46	3.25	0.03
π	0.6–0.8	0.120.16	3.47	2.85	3.66	−0.02
π	0.95–0.97	0.42–0.56	2.56	4.81	3.31	−0.01
p	0.6–0.8	0.80–1.06	2.02	5.40	2.82	−0.05
π	0.6–0.8	0.12–0.16	3.47	2.85	3.66	−0.02
π	0.985–0.991	0.80–1.06	1.88	5.68	2.90	0.00
			All particles			
K	0.6–0.8	0.42–0.56	2.99	4.97	3.55	0.00
π	0.6–0.8	0.12–0.16	4.52	1.73	4.72	−0.03
π	0.95–0.97	0.42–0.56	2.94	5.03	3.20	−0.01
p	0.6–0.8	0.80–1.06	2.31	6.12	2.88	−0.02
π	0.6–0.8	0.12–0.16	4.52	1.73	4.52	−0.02
π	0.985–0.991	0.80–1.06	2.19	6.20	3.08	−0.01

TABLE III. Mean emission points and pair asymmetries for pions, kaons, and protons with velocity (0.6, 0.8) in central Au + Au simulation. Averaging is done over all pairs in this range. See text for the explanation of "flow" and "scrambled."

	$\langle x^{\pi}_{\rm out}\rangle$	$\langle x^{K}_{\rm out}\rangle$	$\langle x^{p}_{\rm out}\rangle$	$\langle x^{\pi}_{\rm out}\rangle - \langle x^{K}_{\rm out}\rangle$	$\langle x^{\pi}_{\rm out}\rangle - \langle x^{p}_{\rm out}\rangle$	$\langle x^{K}_{\rm out}\rangle - \langle x^{p}_{\rm out}\rangle$
			Flow			
Primordial	2.83	4.47	5.61	−1.64	−2.78	−1.14
Nonprimordial	1.34	7.35	9.19			
All	2.00	5.54	6.69	−3.54	−4.69	−1.15
			Scrambled			
Primordial	−0.04	0.00	−0.03	−0.04	−0.01	0.03
Nonprimordial	0.88	3.17	4.20			
All	0.48	1.20	1.28	−0.72	−0.80	−0.08

lighter particles appear to be, on average, emitted closer to the center of the source.[3]

[3]Note that the values in Table II are calculated vs. the single-particle momentum direction, which is only the approximation of the out direction. Values in Table III are calculated vs. the proper out direction: the total momentum of the pair. Therefore small differences between the shift values in the two tables are to be expected.

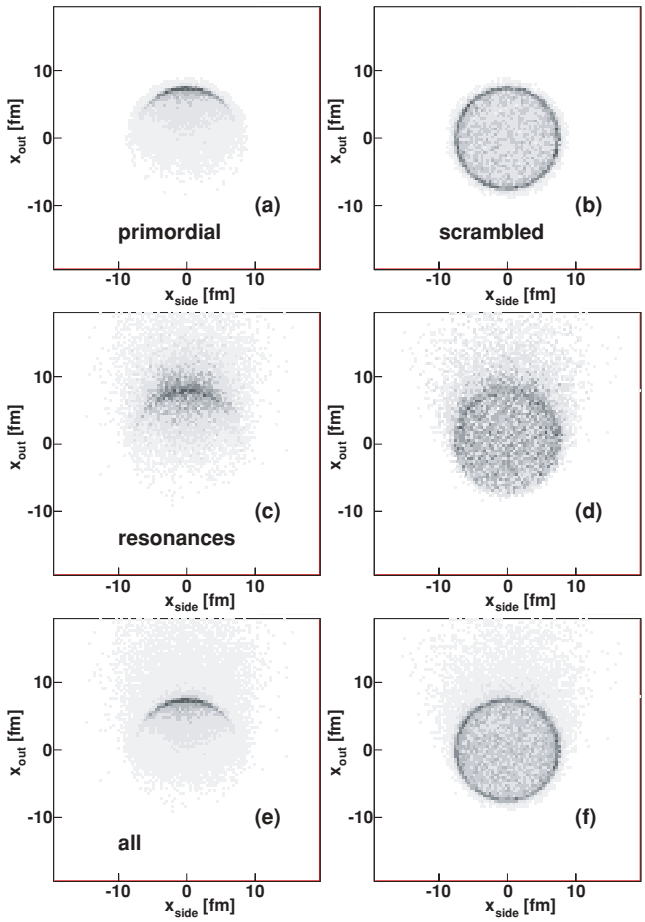

FIG. 2. (Color online) Emission points of particles with a velocity in (0.6, 0.8), their direction pointing "upward," for kaons, central Au + Au. (a, c, e) Standard simulation results; (b, d, f) with flow correlation "scrambled" (see text for details). (a, b) Primordial particles; (c, d) particles coming from resonance decays; (e, f) all particles.

The second trend is the main focus of nonidentical-particle analysis. It so happens that nonidentical-particle femtoscopy correlates particles with *the same velocity* but possibly with *different masses*. Moreover, it has a unique feature of being

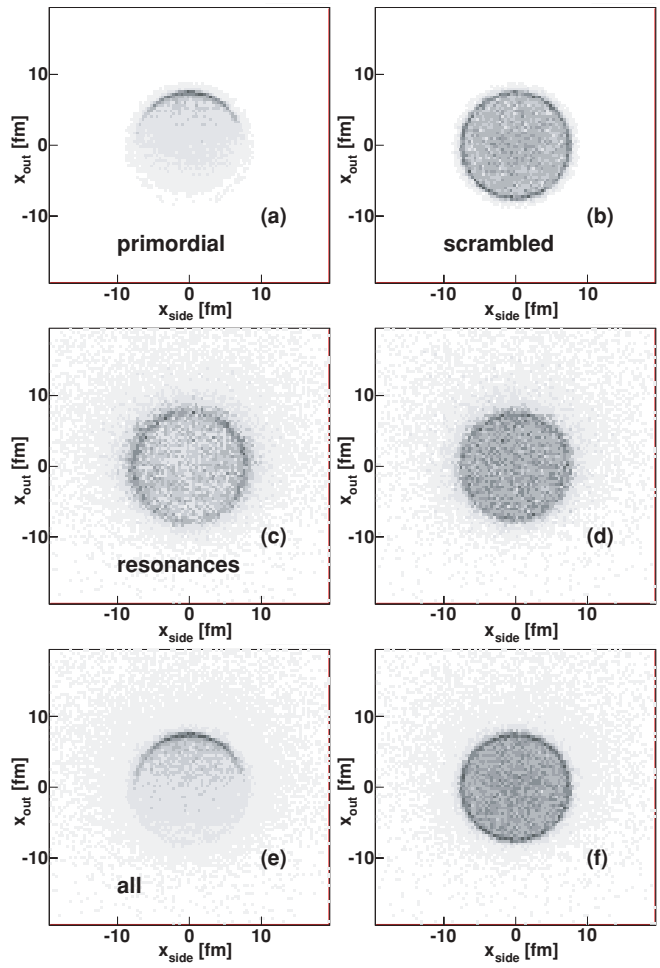

FIG. 3. (Color online) Emission points of particles with a velocity magnitude in the range (0.6, 0.8), their direction pointing "upward," for pions, central Au + Au. Notation is the same as in Fig. 2.

able to measure not only the "size" (more precisely, the second moment of the two-particle distribution—the variance) but also the "shift" (i.e., the first moment of the distribution—the mean) between average emission points. It is therefore able to directly test the predictions of the hydrodynamic model with respect to the x-p correlations. We would like to emphasize that this is the most direct and unambiguous signal of collectivity available to femtoscopy. The m_T scaling, which is predicted by hydrodynamics, can also be explained by other mechanisms not requiring collectivity (e.g., "temperature gradients" [34]); but no mechanism is known that would produce such specific emission asymmetries with no collectivity.

The asymmetry is predicted to arise only in the out direction. The side asymmetry is 0. It can also be shown that for rapidity symmetric systems of a collider, such as the RHIC, when the target is identical to the projectile, the longitudinal asymmetry is also expected to vanish.

B. "No directional correlation" test

In the previous section we have argued that the correlation between the spatial emission angle ϕ_r and the particle's velocity direction ϕ_f is responsible for the emission asymmetries. We tested this argument by performing a calculation in which we intentionally broke this correlation, to show that in such a case no asymmetries arise. We take each *primordial* particle separately. From its original transverse emission coordinates (x_o, y_o), we calculate its transverse emission radius r and angle ϕ_r. Then we randomize the angle ϕ_r, but keep the emission radius r unchanged, and calculate the new "scrambled" emission point (x_s, y_s). If the particle is unstable and consequently decays, the emission points of all daughter particles are shifted by the same amount, calculated for the parent particle $(x_s - x_o,\ y_s - y_o)$. Note that the momentum observables are not affected.

Figures 2–4 show the effect of this procedure on primordial particles. As expected, the average emission point of all particle types is now at $(0, 0)$, and the asymmetry between particles of different masses, listed in Table III, is 0. Our claims are confirmed: the model with no directional correlation shows no asymmetry.

C. Importance of resonances

The LHYQUID + THERMINATOR model assumes that the evolution of the heavy-ion collision proceeds in stages. After the initial nonequilibrium phase there is a collective phase, that can be well described by hydrodynamic equations, with the equation of state assuming the existence of quark-gluon plasma. However, at some point the system becomes so dilute that the continuous medium description of hydrodynamics is no longer viable and one converts the system to hadronic degrees of freedom: the THERMINATOR model does it via the von Neumann sampling of the probability distribution obtained from the Cooper-Frye formula. All known resonances are the degrees of freedom in the hadronic phase. Their abundances are well described by chemical models, and if one trusts these calculations, then at least two-thirds of the observed pions do not come from the original hydrodynamic phase (the so-called primordial particles) but are daughters of resonances. Additionally, all resonances have their intrinsic lifetime, so

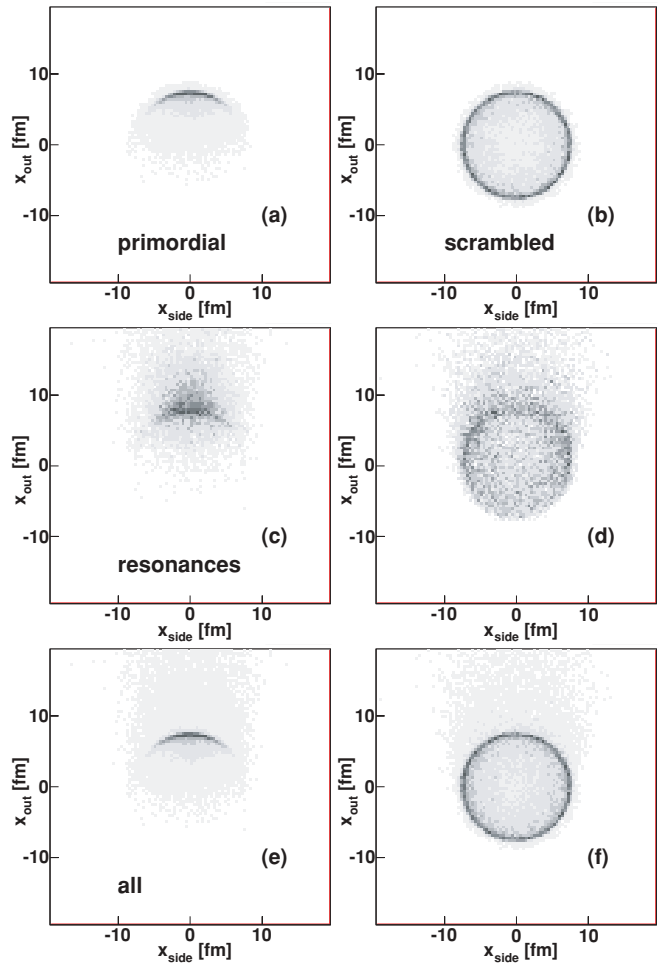

FIG. 4. (Color online) Emission points of particles with a velocity in (0.6, 0.8), their direction pointing "upward," for protons, central Au + Au. Notation the same as in Fig. 2.

they travel some distance before decaying—hence they will certainly modify the space-time picture of particle emission. It is clear that a careful and detailed simulation of the resonance propagation and decay (e.g., as implemented in THERMINATOR) is a critical feature of the model, which aims to describe femtoscopic observables. Also, the relative abundances and decay momenta of resonances producing pions, kaons, and protons as final particles are obviously quite different; so, the feature is even more important for nonidentical-particle correlations, where we study relative differences between various particle types.

Let us first qualitatively consider a resonance decay process. We have the original resonance, produced as a primordial particle. Its emission follows the common "flow" x-p correlation, as for any other particle. Resonances are usually quite heavy, so we expect this correlation to be strong. The resonance travels some distance with the original velocity; this enhances the x-p correlation. After some random time the decay process occurs. Two (or three) particles are created at the decay point. We note the similarity between the resonance decay process and the emission from the fluid element. The daughters of the resonance will have a "common" velocity: this time it is

not the fluid element's velocity, but simply the resonance's velocity. And they will have a "random" component—the "decay momentum" of the given decay channel. And again, the random component will matter more for the lighter particle: the velocity that corresponds to the fixed "decay momentum" will be larger for the lighter particle. One can imagine two scenarios. If the decay momentum of the given decay channel is large, compared to the daughters' mass, then the daughters' emission direction will be randomized, and the common x-p correlation will be lost. In contrast, if the decay momentum is small, the correlation will be preserved (or, in other words, the daughter particle will travel in roughly the same direction as the parent) or even enhanced, owing to the additional x-p correlation resulting from resonance propagation.

From the preceding description one concludes that the resonance process will induce the space-momentum correlation in a way similar to the collective flow; so, one can ask if it could be an alternative mechanism producing such asymmetries. However, qualitative expectations for values of the asymmetries or even general trends are not immediately obvious. They will nontrivially depend on the relative abundances of resonances and their daughters, as well as particular values of decay momenta in specific decay channels. The fact that some resonances decay in cascades makes it even more complicated [75]. Moreover, the original primordial resonances will have a natural x-p correlation coming from the earlier hydrodynamic phase. One then faces a quantitative problem: Do the resonance decays introduce emission asymmetries on their own, independent of flow asymmetries? And if yes, how big are they, compared to the asymmetries coming from the flow? In particular, are they small enough that one can still safely interpret the asymmetry observed in the experiment as coming from collective behavior such as flow?

To answer these questions a detailed simulation is needed, in particular, one that has intrinsic x-p correlations coming from flow (preferably with the possibility to switch them off) and that incorporates all known resonances, together with the state-of-the art knowledge of their masses and decay channels. From this description it is clear that the THERMINATOR model is perfectly suited for the task. In addition, we use the scrambling procedure described in the previous section to switch off the x-p correlations coming from flow, to estimate the asymmetry coming from the decay processes alone.

Let us see the effect of resonance decays on the properties of the emitting regions. In Figs. 2(a), 3(a), and 4(a) the emission points of all particles (both primordial and from resonances) are shown, while Table II reports the numerical values of sizes and shifts. The resulting asymmetries are listed in Table III. We consider the size of the system first. As expected, the overall size is larger: this is naturally expected, as the resonances travel some distance before they decay. The m_T scaling seems to be preserved. In general the trend is consistent with previous studies of resonance influence on femtoscopic observables [53,75] and agrees with the natural expectations. Less trivial and more interesting effects are visible in the average emission points. A qualitatively different effect is seen for pions than for kaons and protons. We first inspect the emission points for particles coming from resonances only (no primordial ones), shown in Figs. 2(c), 3(c), and 4(c). For pions the average emission point is shifted *less* from the center for resonance daughters than for primordial ones. Apparently the first scenario, described previously, is in effect here: the decay momenta of the resonances producing pions are so large, compared to the pion mass, that they completely wash out the original flow x-p correlation. In contrast, for both kaons and protons the resonance daughters are shifted *more* from the center than primordial particles. This time the second scenario is in effect: the decay momenta are small compared to the particles' masses, so small, in fact, that they are not even able to counter the additional x-p correlation coming from resonance propagation. A more detailed discussion of this effect, with examples of particular resonances and decay channels for pions and kaons, is given in Ref. [76]. The effect persists when one takes all particles, primordial and resonance daughters, together. Both effects collaborate in enhancing the pion-kaon and pion-proton asymmetries:

$$\begin{aligned} \langle r_{\text{out}}^{\pi K} \rangle &\approx \langle x_{\text{out}}^{\pi} \rangle - \langle x_{\text{out}}^{K} \rangle , \\ \langle r_{\text{out}}^{\pi p} \rangle &\approx \langle x_{\text{out}}^{\pi} \rangle - \langle x_{\text{out}}^{p} \rangle , \end{aligned} \tag{7}$$

while the kaon-proton asymmetry stays rather similar to the primordial-only case (and small):

$$\langle r_{\text{out}}^{Kp} \rangle \approx \langle x_{\text{out}}^{K} \rangle - \langle x_{\text{out}}^{p} \rangle . \tag{8}$$

We compare the source distributions on the left side in Figs. 2–4 to the ones on the right, where the scrambling procedure was applied. The numerical values for asymmetries are listed in Table III. First, let us focus on pion-kaon and pion-proton pairs. As already discussed, scrambled primordial particles show no asymmetry. Nonprimordial particles do show some, but it is still significantly lower than that of non-scrambled ones. This shows that for nonprimordial particles *both* sources of asymmetry are important: the original x-p correlation of the parent particle and the additional asymmetry from the decay process. However, the former dominates. A critical test is the comparison of asymmetries for all particles between the normal flow and the scrambled scenarios, as this is the observable measured in the experiment. As the simulation shows, the asymmetry that can be attributed solely to the trivial resonance decay processes can account for only 20% (17%) of the total asymmetry produced in central Au + Au collisions at the top RHIC energy for the pion-kaon(pion-proton) pair. For kaon-proton pairs the additional asymmetry produced by the resonance decays is negligible.

In summary, we have shown that resonance decays do not dilute but, rather, enhance the asymmetry signal for pion-kaon and pion-proton pairs. At the same time, even though the resonance decay process can potentially be an independent source of emission asymmetry, we have shown, by detailed calculations, that under realistic conditions such asymmetry is less than a quarter of that produced by flow. Therefore our original expectation holds: if significant emission asymmetry is observed in pion-kaon and pion-proton correlations in the experiment, it favors the explanation of strong x-p correlations in the emitting system, such as those produced by hydrodynamic radial flow.

D. Flow-versus-time asymmetries

As noted in Sec. I, the nonidentical-particle correlations technique was initially developed to measure mainly the emission time differences between various particle species. Only later was the connection to radial flow noted [9,35].

In Au + Au collisions one expects intrinsic time differences for at least two reasons. The reader is referred to Ref. [50], where the evolution of the average emission times with the particle's p_T is discussed. It is noted there that, owing to the particular features of the hydrodynamic emission function, particles with a larger p_T were, on average, emitted earlier. In addition, studies with the "blast-wave" parametrization [42] showed that a time difference between particles of different masses arises in boost-invariant models (the influence of the violation of boost invariance on the time and longitudinal shifts is discussed in Ref. [74]). In our case both effects would contribute to the additional asymmetry in the PRF:

$$r^*_{\rm out} = \gamma_t \left(r_{\rm out} - \beta_t \Delta t\right), \tag{9}$$

which would go *in the same direction* as the spatial one coming from radial flow. Even though it cannot be directly correlated with the radial flow, it is still very much hydrodynamic in nature and we do not consider it as an alternative, noncollective explanation of the asymmetry.

However, the resonance decay process can also introduce additional time asymmetries, as resonance decays occur with a certain time delay, and if some particles are more abundantly produced by resonances than others, asymmetries may arise. In contrast to the effect discussed in the previous paragraph, these time delays are not hydrodynamic in nature and should be treated as alternative sources of asymmetry. Moreover, one expects pions to be most abundantly produced by resonance decays, which would mean that they would appear to be, on average, produced later than kaons and protons, producing asymmetry *in the same direction* as the flow. Clearly the matter requires careful quantitative study.

Figures 5(a) and 5(b) show the time and space emission asymmetries. One sees that both are present and are significant. Resonance decays modify both distributions and add a complication of long-range tails. Therefore, the simple mean of a distribution is no longer a good variable to characterize such asymmetries. One is forced to use the mean values of the functional forms fitted to the distributions around the peak. Table IV reports a summary of these fits. We see that even for the primordial particles only, there is already a time difference, although it is smaller than the space one. Introducing resonances increases the time asymmetry. Evidently the expected effect is seen. Comparing the values in the PRF we take the difference between the "all" and the primordial cases for the time asymmetry as an estimate of how much time asymmetry the resonance decays introduce. For both pion-kaon and pion-proton pairs the "nonhydrodynamic" asymmetry coming purely from resonance time delay is less than 15% of the predicted overall asymmetry. For kaon-proton pairs it is less than 25%. Again, the flow asymmetry dominates the calculated asymmetry signal.

TABLE IV. Time and space asymmetries (from the fits to the distributions around their peaks) for central Au + Au collisions. PRF values are indicated by the asterisk.

	$\langle r_{\rm out}\rangle$	$\langle\gamma_t\rangle\langle r_{\rm out}\rangle$	$\langle\Delta t\rangle$	$-\langle\beta_t\rangle\langle\gamma_t\rangle\langle\Delta t\rangle$	$\langle r^*_{\rm out}\rangle$
πK					
All	−3.3	−5.0	2.7	−3.0	−8.0
Primordial	−1.6	−2.4	1.5	−1.7	−4.1
πp					
All	−4.0	−5.7	3.8	−3.5	−9.2
Primordial	−2.4	−3.4	2.1	−2.0	−5.4
Kp					
All	−0.8	−1.1	0.9	−0.6	−1.7
Primordial	−1.0	−1.3	0.5	−0.4	−1.7

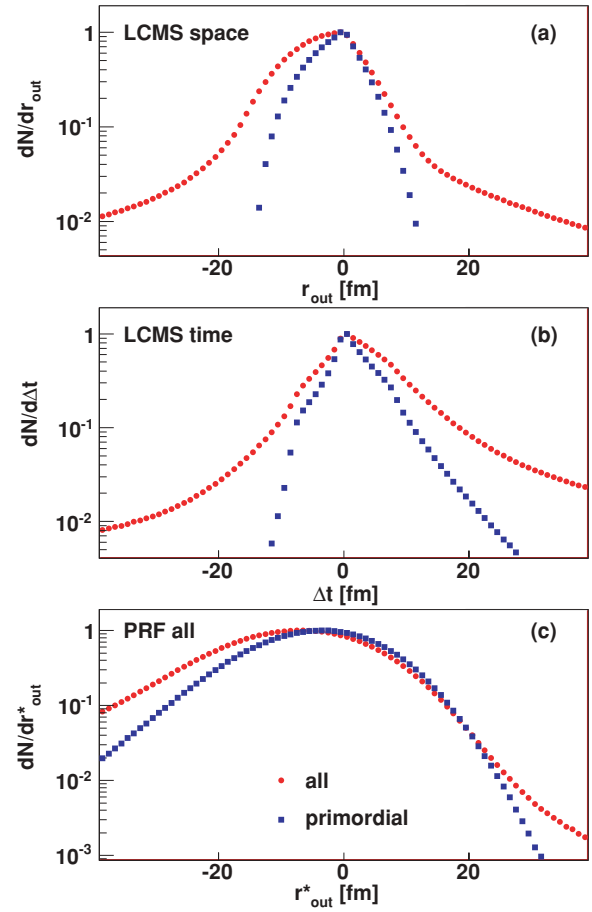

FIG. 5. (Color online) Pion-kaon emission functions in an LCMS for (a) space and (b) time components, combined into the observable asymmetry (c) in the PRF. Circles (red) are for all particles; squares (blue) for primordial particles only.

E. Expectations for qualitative trends

Following the discussion in the previous subsections, one can formulate several predictions of expected qualitative trends. We consider pions, kaons, and protons in specific p_T windows, corresponding to the acceptance of the STAR experiment at the RHIC. This means that the velocities of these particles will be fixed, and one may assume that the same pions

will be correlated with kaons for the pion-kaon correlation and with the protons for the pion-proton correlation. Because we are correlating particles with similar velocities, we will be correlating very low-p_T ($\approx$0.1 GeV/c) pions with medium-p_T kaons ($\approx$0.5 GeV/c) and moderate-p_T protons ($\approx$1 GeV/c). We give a detailed relation between single-particle and two-particle sizes in the Appendix. In terms of the observables themselves, that is, the two particle variances, one expects that $R_{\pi K}$ and $R_{\pi p}$ will be similar and large, as they are dominated by the large low-p_T pion size. In contrast, R_{Kp} is expected to be significantly smaller.

The asymmetries show a common feature, that is, by the definition in Eqs. (7) and (8) (the lighter particle always taken as first), they are all negative: this reflects the fact that lighter particles are expected to be emitted closer to the center of the system than heavier ones.

As for the relations between asymmetries, hydrodynamics naturally predicts that the $\mu_{\pi p}$ will be the largest, $\mu_{\pi K}$ will be of a similar magnitude but smaller, and μ_{Kp} will be much smaller than the other two. It can also be shown that the following relation should hold:

$$\mu_{\pi p} = \mu_{\pi K} + \mu_{Kp}. \tag{10}$$

The asymmetries for all particles for pion-kaon and pion-proton pairs should be significantly different than for primordial particles only, while for kaon-proton pairs the difference should be small.

In Figs. 6, 7, and 8 the predicted system size and emission asymmetry for pion-kaon, pion-proton, and kaon-proton pairs, respectively, calculated by LHYQUID + THERMINATOR, are shown. All the expected trends mentioned in this section are confirmed.

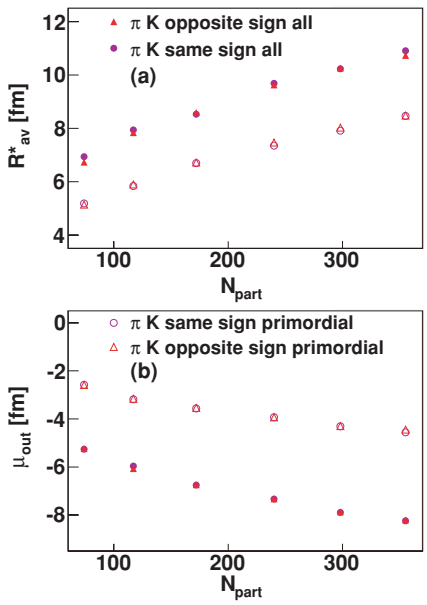

FIG. 6. (Color online) (a) Pion-kaon overall radius and (b) emission asymmetry in the PRF as a function of centrality for Au + Au collisions at $\sqrt{s_{NN}} = 200$ GeV. Filled symbols represent all particles; open symbols, primordial particles only. Circles denote same-sign pairs; triangles, opposite-sign pairs.

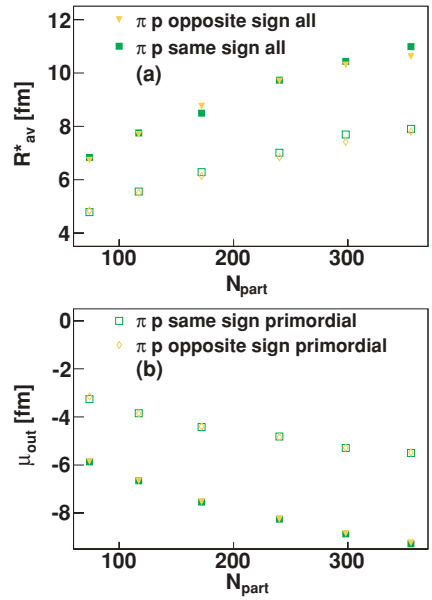

FIG. 7. (Color online) (a) Pion-proton overall radius and (b) emission asymmetry in PRF as a function of centrality. Filled symbols represent all particles; open symbols, primordial particles only. Squares denote same-sign pairs; triangles and diamonds, opposite-sign pairs.

F. Centrality dependence

We first consider the centrality dependence of the system size. The assumed initial conditions have a clear dependence: the system size and initial temperature grow with N_{part}; both should result in larger sizes throughout the evolution. The hydrodynamic evolution assumes identical equation of states and identical freeze-out temperatures for all centralities, so

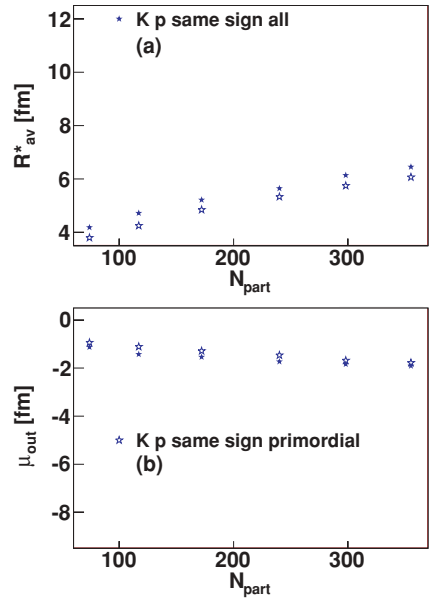

FIG. 8. (Color online) (a) Kaon-proton overall radius and (b) emission asymmetry in the PRF as a function of centrality. Filled symbols represent all particles; open symbols, primordial particles only.

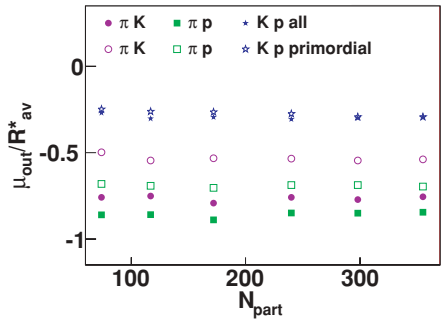

FIG. 9. (Color online) The emission asymmetry scaled by the overall system size in the PRF. Filled symbols represent all particles; open symbols, primordial particles only. Circles denote pion-kaon pairs; squares, pion-proton pairs; and stars, kaon-proton pairs.

there is no reason to expect that this dependence will be altered in the final state. Also, calculations for identical pions show the same trend. Finally, all available experimental data, including pion, kaon, and proton femtoscopy, show the same trend. Therefore an increase in the system size with N_{part} is expected.

The asymmetry is the result of a hydrodynamic evolution. As already mentioned, the parameters of the evolution do not change with centrality, only the initial conditions. Because the chemical properties of matter do not depend on centrality either, the resonance decay phase is not expected to be very different, giving an enlargement of the system size by a constant amount. In contrast, as the collisions become more peripheral, the initial overlap region shrinks, so one expects that the long-range resonance corona will become relatively more important. Because we know that the overall size of the system grows with centrality, the absolute value of asymmetry will also grow. The ratio of asymmetry to the system size is shown in Fig. 9, and indeed we can see that the scaling of μ with R^*_{av} holds well for all centralities and all pair types, for both all and primordial-only particles.

IV. NONIDENTICAL-PARTICLE FEMTOSCOPY FORMALISM

In femtoscopy one aims to measure the space-time configuration of the emission process in hadronic collisions by analyzing the specific behavior of the two-particle correlation function. A natural variable versus which this correlation is measured is half of the generalized pair relative momentum k^*, as opposed to analyses focused on event structures, which use, for example, azimuthal angle and pseudorapidity differences. k^* is calculated in the PRF, so it is also the momentum of the "first" particle of the pair in the PRF. The particles in the pair are different, so it is important to define which one is "first." Later we give the conventions that we use in this paper. Femtoscopy also requires a precise knowledge of particle type, which means that experiments intended to do such an analysis must have a good particle identification capability.

The correlation function is defined as

$$C(\boldsymbol{p}_a, \boldsymbol{p}_b) = \frac{P_2(\boldsymbol{p}_a, \boldsymbol{p}_b)}{P_1(\boldsymbol{p}_a)P_1(\boldsymbol{p}_b)}, \tag{11}$$

where P_2 is the conditional probability of observing a particle with momentum $\boldsymbol{p}_b$ if a particle of momentum $\boldsymbol{p}_a$ is also observed, while P_1 is the simple probability of observing a particle with a given momentum. Note that this definition is general and applies equally well to the femtoscopic correlation function and to other two-particle correlations, for example, event structure ones.

The experimental femtoscopic correlation function is a specific form of Eq. (11), written as

$$C(\boldsymbol{k}^*) = \frac{\int A(\boldsymbol{p}_a, \boldsymbol{p}_b)\delta\left(\boldsymbol{k}^* - \frac{1}{2}(\boldsymbol{p}^*_a - \boldsymbol{p}^*_b)\right)d^3p_a d^3p_b}{\int B(\boldsymbol{p}_a, \boldsymbol{p}_b)\delta\left(\boldsymbol{k}^* - \frac{1}{2}(\boldsymbol{p}^*_a - \boldsymbol{p}^*_b)\right)d^3p_a d^3p_b} \equiv \frac{A(\boldsymbol{k}^*)}{B(\boldsymbol{k}^*)}, \tag{12}$$

where $A(\boldsymbol{p}_a, \boldsymbol{p}_b)$ is the distribution of correlated pairs (i.e., both particles coming from the same event) of particles of types a and b, and $B(\boldsymbol{p}_a, \boldsymbol{p}_b)$ is the same distribution, but the particles are not correlated (i.e., they come from two different events). Note that the argument of C is changed to half of the pair relative momentum k^*. Also note that with this definition the correlation function will contain not only femtoscopic correlations, but also all other eventwide correlations projected to the two-particle space. These include the elliptic flow v_2, global event energy and momentum conservation, resonance decay correlations (if a and b are different and could be products of the decay of a given resonance, for example, products of the Δ^{++} resonance in the π^+-p correlation function), residual correlations (remnants of the femtoscopic correlations between parent particles, which decayed weakly into the particles of interest, for example, residual correlations between Λ and p feeding into the p–p correlations), jets, etc. There are numerous experimentalist recipes for constructing B in such a way that these correlations are included there. In that case, dividing A and B also divides out the correlations. One should also correct for other nonfemtoscopic effects, so that one is left with a pure femtoscopic correlation in C. The latter is desirable, as it is the femtoscopic-only effect that is usually computed in models. But such correction procedures are never fully effective, so one must take this into account when comparing the "compound" correlation functions from the experiment with the "pure" femtoscopic correlation function from models. The details of such procedures are clearly experiment dependent and are beyond the scope of this paper. We only note that some models may include the effects of global correlations (e.g., elliptic flow and energy-momentum conservation), so they can be used to model such effects. We discuss how this can be done later.

In models one defines the correlation function via the single- and two-particle emission functions:

$$S_A(\boldsymbol{x}_1, \boldsymbol{p}_1) = \int S(x_1, p_1, x_2, p_2, \ldots, x_N, p_N) \times dx_2 dp_2 \cdots dx_N dp_N, \tag{13}$$

$$S_{AB}(\boldsymbol{x}_1, \boldsymbol{p}_1, \boldsymbol{x}_2, \boldsymbol{p}_2) = \int S(x_1, p_1, x_2, p_2, \ldots, x_N, p_N) \times dx_3 dp_3 \cdots dx_N dp_N, \tag{14}$$

which are interpreted as the probability of emission of a particle (or a pair of particles) from a given space-time point with a given momentum. With this definition one might substitute S_{AB} for P_2 and S_A for P_1 in Eq. (11). Such a correlation function is a 14-dimensional object (7 independent components per particle: 4 space-time and 3 momenta). Assumptions are needed to reduce the number of dimensions. We describe them here.

In principle, the source emission function S_{AB} should reflect all the physics aspects of the particle emission process, including the proper symmetrization for bosons and fermions, as well as the influence of the two-body and many-body FSIs. However, commonly used heavy-ion collision models do not include these effects. Instead, one assumes that each particle's emission process is independent or, in other words, that an interaction between the two final-state particles after they are created is independent of their emission process. The introduction of this factorization of the FSI and two-particle wave function symmetrization gives the equation

$$C(\boldsymbol{p}_1, \boldsymbol{p}_2) = \int S_{AB}(\boldsymbol{p}_1, \mathbf{x_1}, \boldsymbol{p}_2, \mathbf{x_2}) \, |\Psi_{AB}|^2 \, d^4\mathbf{x_1} d^4\mathbf{x_2}, \quad (15)$$

where Ψ is the pair wave function. Particle types A and B are known, so the momenta have only three independent components, while for positions all four components are independent. We also mention that Eq. (15) has strong similarities to the Fermi equation used to describe the β decay process [77].

A. Pair wave function

The pair wave function Ψ describes the behavior of a pair of particles, one of type A and the other of type B. In nonidentical-particle correlations we use a particular form of Ψ, which corresponds to the following physical scenario: two particles A and B, which, shortly after they are produced in a heavy-ion collision, interact via the FSI, in our case Coulomb and/or strong. After this interaction they propagate to the detector as plane waves. In that case, the particular form of Ψ is the solution of the scattering problem, viewed in the reversed time direction. We also use an equal-time approximation, which assumes that the particles were born at the same time in the PRF (see Refs. [10] and [14] for a detailed description and estimation of the systematic error introduced by this assumption). We factorize the wave function into a part describing the motion of the pair as a whole (a function of the pair total momentum and "average" emission point) and a component describing the interaction itself—dependent on the pair relative momentum $\boldsymbol{k}^*$ and separation $\boldsymbol{r}^*$. The first component produces only an additional phase, which does not influence the modulus of the wave function. Because in our study we are only interested in the modulus, we can neglect this component, and we are left with [10]

$$\Psi^{(+)}_{-k^*}(\mathbf{r}^*) = \sqrt{A_C(\eta)} \left[e^{-i\mathbf{k}^*\mathbf{r}^*} F(-i\eta, 1, i\zeta) + f_C(\boldsymbol{k}^*) \frac{\tilde{G}(\rho, \eta)}{\mathbf{r}^*} \right], \quad (16)$$

where A_C is the Gamow factor, $\zeta = k^* r^* (1 + \cos\theta^*)$, $\eta = 1/(k^* a_C)$, F is the confluent hypergeometric function, $\tilde{G}$ is the combination of the regular and singular S-wave Coulomb functions, and f_C is the strong scattering amplitude, modified by the Coulomb interaction. θ^* is the angle between the pair relative momentum k^* and the relative position r^* in the PRF, while a_C is the Bohr radius of the pair, equal to 248.52, 222.56, and 83.59 fm for pion-kaon, pion-proton, and kaon-proton pairs, respectively, and is negative for opposite-charged pairs. For identical particles, Ψ must also be properly (anti-)symmetrized. This equation is valid in the outer regions of the strong interaction potential and neglects the components for angular momentum $l \geqslant 1$; the latter is a valid approximation for small k^*.

In femtoscopic analysis we assume that we know Ψ with infinite accuracy, so that we can try to invert Eq. (15) to obtain, from the measured correlation function C, information about the emission function S_{AB}. In this work we focus on nonidentical combinations of the most abundant stable hadrons measured in heavy-ion collisions: pions, kaons, and protons. For each of the combinations (pion-kaon, pion-proton, and kaon-proton), there are four charge combinations: two of the same sign and two of the opposite sign. The wave function for both same-sign (and both opposite-sign) combinations are identical. We note that the wave function characteristics are indeed well known for all combinations, except for the opposite-sign kaon-proton pair. The strong interaction in this system is interesting in its own right and is the focus of intense theoretical investigation (see, e.g., Ref. [78]). The femtoscopy technique can be useful in this regard—by inverting the problem and assuming that we know the source distribution (from other femtoscopic measurements), we can invert Eq. (15) to deduce the parameters of Ψ from the measured correlation function. Similar technique can also be used to study the strong interaction in the $\pi^+\pi^-$ system precisely. Such studies are beyond the scope of this paper (see, e.g., Refs. [10] and [74]).

For the systems analyzed in this work, f_C can be parametrized in the effective range approximation by

$$f_C(\boldsymbol{k}^*) = \left[\frac{1}{f_0} + \frac{1}{2} d_0 \boldsymbol{k}^{*2} - \frac{2}{a_C} h(\boldsymbol{k}^* a_C) - i\boldsymbol{k}^* A_C(\boldsymbol{k}^*) \right]^{-1}, \quad (17)$$

where f_0 is 0.137 fm for the same-sign pion-kaon pair, -0.071 fm for the opposite-sign pion-kaon pair, -0.148 fm for same-sign pion-proton pair, 0.112 fm for opposite-sign pion-proton pair, and -0.360 fm for the same-sign kaon-proton pair. The effective radius d_0 can be put equal to 0 for all considered pairs at small k^* where the $1/f_0$ term dominates.

The full form of the wave function, Eq. (16), must be used when calculating correlation functions to be compared with data. However, for theoretical calculations it is sometimes instructive (and faster numerically) to neglect the strong interaction. This is acceptable, as the strong interaction is expected to be small for the pairs of interest, except for opposite-sign kaon-proton pairs, which we do not include in the model calculations. For simplicity we use the Coulomb-only wave function in the discussion in the next paragraph, but

the conclusions hold for the full Coulomb + strong calculation as well.

For the discussion it is important to provide the form of the F function explicitly:

$$F(\alpha, 1, z) = 1 + \alpha z + \alpha(\alpha+1)z^2/2!^2 + \cdots. \quad (18)$$

B. Emission function

The FSI correlation, described by Eq. (16), depends only on the relative momentum $\boldsymbol{k}^*$ and separation $\mathbf{r}^*$ of the pair (the angle between the two vectors is θ^*). The first simplification of S_{AB} from Eq. (14) is to change to the relative variables and integrate out the sum ones:

$$\begin{aligned} S_{AB}(\boldsymbol{k}^*, \mathbf{r}^*) = \int\!\!\int_{P_{\min}}^{P_{\max}} & S_{AB}(\mathbf{x}_1, \boldsymbol{p}_1, \mathbf{x}_2, \boldsymbol{p}_2) \\ & \times \delta(\boldsymbol{k}^* - 1/2(\boldsymbol{p}_1^* - \boldsymbol{p}_2^*))\, d^3p_1 d^3p_2 \\ & \times \delta(\boldsymbol{r}^* - (\boldsymbol{x}_1^* - \boldsymbol{x}_2^*))\, d^4x_1 d^4x_2. \end{aligned} \quad (19)$$

The integration over space is done over the full variable range. In contrast, particles' momenta are measurable, so it is possible to define the boundary momenta $P_{\min}$ and $P_{\max}$ for which the integration is done. In fact, for identical-particle femtoscopy it is common to define several $k_T = 1/2(p_T^1 + p_T^2)$ ranges and create separate correlation functions for each of them. In this way, the information about the P dependence of S_{AB} is not completely integrated out and can still be inferred. Up to now similar binning was not possible for nonidentical-particle correlations at the RHIC, because of small statistics and limited p_T acceptance with good particle identification coverage. However, when one compares the model and the experiment data, one must take care to restrict the P integration range at least to the one dictated by the p_T acceptance of the experiment.

The emission function, Eq. (19), is a seven-dimensional object. We use it to rewrite equation (15), using the specific form of the wave function, Eq. (16), as well:

$$C(\boldsymbol{k}^*) = \int S_{AB}(\boldsymbol{k}^*, \mathbf{r}^*) \left|\Psi_{-k^*}^{(+),AB}(\mathbf{r}^*)\right|^2 d^4\mathbf{r}^*. \quad (20)$$

This form can be explicitly used to calculate the correlation function from models. However, it is very rare for a model to provide the full two-particle emission function. The existing models fall into two categories: either they provide an analytic form of a *single-particle* emission function or they provide information only about the produced particles.

In the first case we assume that each particle's emission process is independent. Then the two-particle emission function S_{AB} can be constructed from single-particle emission functions via a convolution:

$$\begin{aligned} S_{AB}(\boldsymbol{k}^*, \mathbf{r}^*) = \int & S_A(\boldsymbol{p}_1, \mathbf{x}_1) S_B(\boldsymbol{p}_2, \mathbf{x}_2) \\ & \times \delta\left(\boldsymbol{k}^* - \frac{1}{2}(\boldsymbol{p}_1 + \boldsymbol{p}_2)\right) \delta(r^* - \mathbf{x}_1 + \mathbf{x}_2) \\ & \times d^4\mathbf{x}_1 d^4\mathbf{x}_2 d^3\boldsymbol{p}_1 d^3\boldsymbol{p}_2. \end{aligned} \quad (21)$$

In the case of identical particles ($A \equiv B$), several simplifications can be made. The convolution of two identical Gaussians is also a Gaussian with σ multiplied by $\sqrt{2}$. Femtoscopy can provide information about the two-particle emission function only, but with the preceding simplifying assumption, the σ of the single-particle distribution can be inferred. For nonidentical particles, $A \neq B$, the simplified method of comparison is not applicable. The comparisons with models is more complicated, but retrieving single-particle source sizes is still possible, provided a complete set of measurements is performed. The formula is used in Sec. VII and derived in the Appendix. Also, because generally $S_A \neq S_B$, the S_{AB} can yield a nonzero mean value of the separation vector $\langle \boldsymbol{r}^* \rangle$. Later in this section we explain how this mean value can be accessed experimentally and argue that this is an important and unique piece of information accessible via nonidentical-particle femtoscopy only.

In the second case, a model discretely producing particles, Eq. (20), is evaluated via the Monte Carlo procedure:

$$C(\boldsymbol{k}^*) = \frac{\sum_{\text{pairs}} \delta(\boldsymbol{k}_{\text{pair}}^* - \boldsymbol{k}^*) \left|\Psi_{-k^*}^{(+),AB}(\mathbf{r}^*)\right|^2}{\sum_{\text{pairs}} \delta(\boldsymbol{k}_{\text{pair}}^* - \boldsymbol{k}^*)}. \quad (22)$$

Note that if the particles from the model are produced in a correlated way (e.g., with energy and momentum conservation for the full event, with energy and momentum conservation for resonance decay, etc.), these are *not* destroyed and are still present in C. In other words, this method does not require the simplifying assumption of Eq. (21). In this work we use this method to calculate model correlation functions. Its practical implementation is described in Sec. V.

C. Correlation function and asymmetry signal

Equation (15) essentially defines the correlation function as a pair wave function averaged over the source. Using the simplified wave function containing only the Coulomb part, one can write

$$C(k^*) = A_C(\eta)[1 + 2\langle r^*(1 + \cos\theta^*)\rangle/a_c + \cdots], \quad (23)$$

where averaging is done over pairs. In this example we illustrate the origins of the asymmetry effect by considering same-sign pion-kaon pairs. In this case, a_c is positive, A_C is negative, and $r^*(1 + \cos\theta^*)$ is by definition always positive. For a point source ($r^* = 0$) the overall correlation effect $R = |C - 1|$ would be maximum and equal to $1 - A_C$. For our pairs $A_C - 1$ is negative, while $2\langle r^*(1 + \cos\theta^*)\rangle/a_c$ is positive, so the two compete with each other. As the size of the system grows, so does the average r^*, and the correlation effect R decreases. Therefore, the correlation function is sensitive to the source size, so we expect to be able to measure the size of the system. One has to remember that as the size grows, the correlation function gets less and less sensitive to the system size; therefore, the analysis is able to accurately measure only sizes that are not too large. To determine whether "too large" is larger than the maximum expected system size at the RHIC is one of the objectives of this paper. Figure 10 shows an example of how a nonidentical particle correlation function (in this case same-sign pion–kaon) depends on the size of the system. One can see that for a reasonable system size (comparable to the maximum femtoscopic sizes obtained in the central

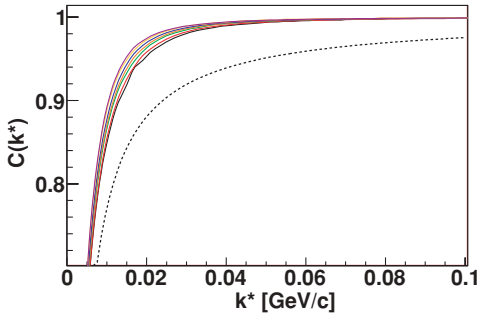

FIG. 10. (Color online) An example of the nonidentical-particle correlation function dependence on the size of the system. Solid lines represent same-sign pion-kaon correlation functions for a Gaussian source with σ from 7.0 fm (lowest) to 13 fm (highest) and a shift of -5 fm. The Gamow factor is shown as the dashed line for comparison.

Au + Au collisions at the RHIC), there is a noticeable and monotonic dependence on the size, indicating that a qualitative femtoscopic analysis should be possible.

As mentioned in the previous paragraph, the two-particle emission function can yield a nonzero mean value of the separation vector $\langle \mathbf{r}^* \rangle$. We now discuss how it can be observed in the data. From Eq. (23) the correlation function depends on the angle θ^*, between relative momentum $\boldsymbol{k}^*$ and relative position $\boldsymbol{r}^*$. When the two are aligned ($\cos\theta^* > 0$), the correlation effect is smaller than when they are antialigned ($\cos\theta^* < 0$). The former configuration means that the particles of the pair, when born, immediately start to fly away from each other, so their effective interaction time is shorter. In the latter case, when they start to fly toward each other, they pass close to each other and only later fly away. Angle θ^* is not accessible experimentally, but it does influence R.

Particles' momenta, measured experimentally, can be used to calculate the relative momentum $\boldsymbol{k}^*$ and the pair total momentum $\boldsymbol{K}$, corresponding to the velocity $\boldsymbol{v}$. The angle between the two is ψ. One divides the observed pairs into two groups, one having $\boldsymbol{k}^*$ and $\boldsymbol{v}$ aligned ($\cos\psi > 0$) and the other having $\boldsymbol{k}^*$ and $\boldsymbol{v}$ antialigned ($\cos\psi < 0$), and creates two correlation functions, C_+ and C_-. If, in the pair sample used to calculate the C_+, we have a majority of pairs that also have $\cos\theta^* > 0$ (and in the C_- sample the majority of pairs have $\cos\theta^* < 0$), then C_+ and C_- would differ. In this particular case, C_+ would show a smaller correlation effect and C_- a larger one. When plotting a "double-ratio" C_+/C_-, one would see a signal deviating from unity. For same-sign pairs it would go above unity, while for opposite-sign pairs it would go below unity.

If we see a nonzero double-ratio, it means that $\cos\theta^*$ is somehow correlated with $\cos\psi$. They are connected via a third angle of interest: the angle ϕ between the pair velocity $\boldsymbol{v}$ and the pair relative position $\boldsymbol{r}^*$. When we consider only the projections of all these angles on the transverse plane, we have trivially

$$\psi = \theta^* + \phi. \tag{24}$$

For the average cosines of these angles, we can write

$$\langle \cos\psi \rangle = \langle \cos\theta^* \cos\phi \rangle. \tag{25}$$

By definition, for C_+ the left-hand side of Eq. (25) is positive. We assumed that C_+ shows a larger correlation effect, so $\langle \cos\theta^* \rangle$ is negative. The only way that the equation can be fulfilled is also to have $\cos\phi < 0$. In other words, it is required that, on average, $\boldsymbol{r}^*$ is antialigned with $\boldsymbol{v}$. This is a crucial point, so let us restate it. If we see a nonunity double-ratio, we can conclude that the average relative position direction is correlated with the pair velocity direction. That means that we can access, via a rather straightforward procedure, the mean of the two-particle separation distribution, which is allowed to be nonzero for nondentical particles. The emission asymmetry $\langle \mathbf{r}^* \rangle$ is a three-vector, while the preceding consideration only mentions a single direction (the direction of the pair velocity $\boldsymbol{v}$). The argument is more general: we can replace $\boldsymbol{v}$ with any other direction, defined in the PRF, and repeat the argument to obtain the same conclusions. The simplest generalization, which we have shown to have important physics motivation, is the decomposition of $\boldsymbol{v}$ into components: the longitudinal "long" (along the beam axis) and the transverse "out" (perpendicular to the beam axis). By performing the asymmetry analysis versus these two directions, we can obtain information about the out asymmetry $\mu_{\text{out}} = \langle r^*_{\text{out}} \rangle$ and the long asymmetry $\mu_{\text{long}} = \langle r^*_{\text{long}} \rangle$. For completeness we also use the third direction, "sideward" or "side," perpendicular to the other two to study the side asymmetry $\mu_{\text{side}} = \langle r^*_{\text{side}} \rangle$. Each of them carries important physics information or is useful as an experimental cross-check; the details are discussed in the following sections.

We discussed the possible physical origins of the emission-point asymmetry and its significance in Sec. III. Now we discuss the general properties of the double-ratio observable. It is allowed to go both above and below unity, which means either positive or negative emission asymmetry (the average emission separation being aligned or antialigned with the velocity direction). It can also be unity, meaning no emission asymmetry. More detailed analysis also shows that, for a fixed source size, introducing larger and larger emission asymmetry produces larger and larger deviation from unity of the double-ratio signal. This means that one can determine the existence of emission asymmetry and also measure its magnitude. The technical details of how it is done are presented in the next section. The illustration of the double-ratio behavior, for a fixed system size for a same-sign pion-kaon pair, is shown in Fig. 11.

It is instructive to derive the equation for asymptotic behavior of the double-ratio C_+/C_- at k^* going to 0 [8,9]. We focus on the function F. In this limit, we neglect all components with $1/a_C$ or $1/k^*$ in powers greater than 1. We have

$$F = 1 + 2\frac{r^*}{a_C} + 2\frac{\boldsymbol{k}^*\boldsymbol{r}^*}{k^* a_C} + O\left[\left(\frac{1}{a_C}\right)^2\right] + O\left[\left(\frac{1}{k^*}\right)^2\right] + \cdots, \tag{26}$$

which gives the correlation function:

$$C|_{k^*} = \langle A_C F^* F \rangle \doteq A_C \left(1 + 2\frac{\langle r^* \rangle}{a_C} + 2\frac{\langle \boldsymbol{k}^*\boldsymbol{r}^* \rangle}{k^* a_C}\right). \tag{27}$$

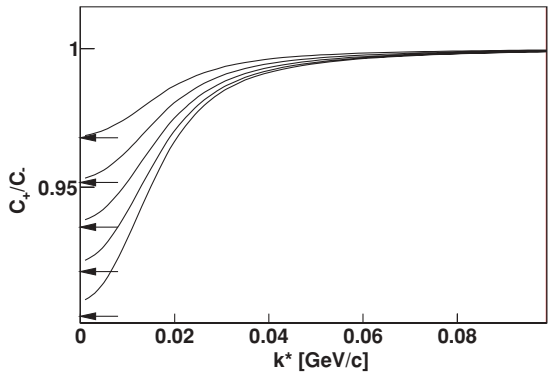

FIG. 11. An example of the nonidentical-particle "double-ratio" dependence on the emission asymmetry. Solid lines represent same-sign pion-kaon double-ratios for a Gaussian source with a σ of 10.0 fm and an asymmetry of -12.0 fm (lowest) to -4 fm (highest). The arrows point to the asymptotic values (see text for details).

One notes that

$$\langle \boldsymbol{k}^* \boldsymbol{r}^* \rangle = \langle k^*_{\rm out} r^*_{\rm out} + k^*_L r^*_L \cos(\theta^* - \psi) \rangle = k^* \cos\psi \langle r^*_{\rm out} \rangle. \tag{28}$$

We now consider C at a fixed k^* and $\cos(\psi)$,

$$C(k^*, \cos\psi) = A_C \left(1 + 2\frac{\langle r^* \rangle}{a_C} + 2\cos\psi \frac{\langle r^*_{\rm out} \rangle}{a_C}\right), \tag{29}$$

and using the uniformity of the $\cos\psi$ distribution for uncorrelated particles at small k^*, we have

$$\begin{aligned} C_+ &\doteq A_C \int_0^1 C(\cos\psi) d\cos\psi = 1 + 2\frac{\langle r^* \rangle}{a_C} + \frac{\langle r^*_{\rm out} \rangle}{a_C}, \\ C_- &\doteq A_C \int_{-1}^0 C(\cos\psi) d\cos\psi = 1 + 2\frac{\langle r^* \rangle}{a_C} - \frac{\langle r^*_{\rm out} \rangle}{a_C}, \\ \frac{C_+}{C_-}|_{k\to 0} &\doteq 1 + 2\frac{\langle r^*_{\rm out} \rangle}{a_C}. \end{aligned} \tag{30}$$

These asymptotic values of the double-ratio are shown as arrows in Fig. 11. The formula appears to give an easy way to extract an emission asymmetry without the need for tedious analysis. However, one must remember that in the experiment, the lower the k^*, the higher the experimental uncertainty on the data point. This is because of statistics, which falls as k^{*2}, and because experimental effects like momentum resolution result in the largest systematic uncertainty in these bins. Therefore, one has to perform the full analysis of the double-ratio over a broad range of k^* to reliably extract the asymmetry.

From Eqs. (30) one concludes that if one restricts the integrals in the definitions of $C_+(C_-)$ to a $\cos(\psi)$ range close to $1(-1)$, one will obtain an even larger asymmetry signal. However, in the experiment, the price to pay is the loss of statistics, and hence the significance of the signal. It can be shown that to maximize the significance of the signal, one should perform the integrals over the full range of $\cos(\psi)$ (thus minimizing the statistical error) with the weight $\cos(\psi)$ [79,80]. We come back to this crucial point in Sec. V A, where we discuss the SH representation of the correlation function, which happens to naturally introduce similar weighting [80,81].

We finish this chapter by discussing the conventions used in the analysis. It is important to define and consistently use these conventions in all steps of the analysis. First, the order of particles in the pair is important for the definition of k^* and r^* because they are defined as the momentum and position of the *first* particle in the pair. We adopt a convention that the lighter particle in the pair is always taken to be first. If both particles have an equal mass, the positively charged one is taken as first. The second convention is the definition of the double-ratio, which can be either C_+/C_- or C_-/C_+. We choose the former definition. We also note that in the SH representation, there is no need for such a convention. With these definitions the following general rules hold. Same-charge pairs have correlation functions going below unity; opposite-charge pairs, above unity. This means that for a given source size asymmetry, the double-ratio for same-sign pairs will be an inverse of the opposite-sign double-ratio. Finally, with these definitions, a double ratio below(above) unity means that the lighter particle is emitted closer to the center of the system and/or later than the heavier one for the same-sign(opposite-sign) pair.

V. PRACTICAL IMPLEMENTATION OF THE FORMALISM

When using a model that produces individual particles (such as THERMINATOR), the integration in Eq. (15) is performed via the Monte Carlo method, iterating over particle pairs. In that case, the procedure to construct the correlation function closely resembles the experimental one. It enables the introduction of some experimental effects, such as acceptance or momentum resolution, in a straightforward way, as opposed to the purely analytical models, where this is more difficult. Mathematically, the procedure is a combination of Eqs. (12) and (15):

$$C(\boldsymbol{k}^*) = \frac{\int A(\boldsymbol{k}^*, \mathbf{r}^*) |\Psi(\boldsymbol{k}^*, \mathbf{r}^*)|^2}{\int B(\boldsymbol{k}^*, \mathbf{r}^*)}. \tag{31}$$

Note that the A and B now depend on space-time coordinates $\mathbf{r}^*$ as well, because we are using model data in which the emission points are known. Because we are dealing with pairs of individual particles, we employ the Monte Carlo procedure, which replaces the analytic integration by summing over pairs:

$$C(\boldsymbol{k}^*) = \frac{\sum_{N\text{pairs}} \delta(k^*_A - k^*) |\Psi(\boldsymbol{k}^*, \mathbf{r}^*)|^2}{\sum_{D\text{pairs}} \delta(k^*_B - k^*)}, \tag{32}$$

where the two sums are performed over two sets of pairs N and D and the δ function ensures that only pairs with the correct relative momentum are taken. Note that there are two possible scenarios, both of which have slightly different interpretations and uses. One can perform the calculation using the same pairs for set N and D. Equation (32) is then exactly equivalent to Eq. (15) but is done via Monte Carlo integration. Another option is to take pairs from the same event as sample N and pairs of particles from different events as sample D. In that case, the correlation function C contains not only the femtoscopic effect but also all other event-wide correlations which are present in the model, projected to the two-particle space. It is therefore very useful for experimentalists, who

can study the differences between the two to estimate the magnitude of the nonfemtoscopic effects. The two cases have one more important difference. Usually the correlation function is constructed as a ratio of two histograms: N, a signal, which is filled with the weight $|\Psi|^2$ for every pair; and D, the background, which is filled with unity for each pair. The error bar on $C = N/D$ has a different meaning in the two cases. In the first one it is just the spread of the weight in a given sample. In the second case it is a true error bar, comparable to the experimental one, as samples N and D are statistically independent. In this work we use the first way to calculate the correlation function, as we are not interested in nonfemtoscopic correlations but, rather, in physics effects accessible via femtoscopy.

A. Correlation function representation

Femtoscopic correlation functions have been represented in two main forms: as a one-dimensional (1D) histogram with the magnitude of the relative momentum k^* or $q = 2k^*$ on the axis or as a three-dimensional (3D) histogram with k^*_{out}, k^*_{side}, and k^*_{long} on the axes. For identical pion correlations it is also useful to use a 3D histogram with the relative momentum components q_{out}, q_{side}, and q_{long} calculated in an LCMS. Note that out, side, and long decomposition is possible also for pairs of nonidentical particles; one has to use the generalized four-momentum variable $\tilde{q}$ instead of q: $\tilde{q} = q - P(qP)/P^2$. The first form requires minimal statistics but allows determination only of the 1D overall source size. The second one allows for the determination of sizes in all three directions but requires significant statistics. Up to now, the nonidentical correlation function was represented as a set of two 1D histograms, one for C_+ and one for C_-, with respect to the out direction. This allowed for the determination of 1D source size and a study of the double-ratio to access asymmetries. However, if one wanted to study double-ratios for other directions (side and long), one would need to create separate sets of correlation functions.

Recently, a more advanced way of representing the correlation function, SH, was proposed [82]. It has several important advantages. It encodes the full 3D information on the correlation in a set of 1D plots. Generally, this does not need to be an advantage, because a perfect representation of all the features of any 3D function requires an infinite set of l, m components (meaning: infinite set of 1D histograms). But it so happens that the intrinsic symmetries of a pair distribution in the femtoscopic analysis result in most of the l, m components vanishing. It has also been shown that, of those that do not vanish, only those with small l contain important information, which means that one can safely truncate the decomposition at a rather small l without the fear of losing any physics information. It is as if the SH have been specifically designed to efficiently represent a femtoscopic correlation function.

The SH representation has the advantages of both the 1D correlation function (because it requires less statistics) and a 3D one (because it encodes the important part of the 3D information). However, first attempts to apply the decomposition methods, which were developed for identical particles, to nonidentical-particle correlations were not successful. Essentially, one had to first construct the numerator and denominator as 3D histograms (usually in $|\boldsymbol{q}|$, $\cos\theta_q$, and ϕ), then divide them and decompose the resulting 3D correlation function, negating the low-statistics advantage of the 1D representation. The decomposition procedure also relied heavily on the symmetries present for identical correlations. This presented a problem for nonidentical correlations, because their primary goal is to study the emission asymmetry. This breaks one of the symmetries present in identical analysis. Also, the single-particle acceptance of some experiments produced "acceptance holes," that is, regions of empty bins in the 3D function. Also, statistics for nonidentical pairs were significantly lower than for pion-pion correlations, so filling all the bins in a 3D correlation function with a significant number of pairs became a challenge. To solve these problems, a new technique to represent the correlation function in SH was developed [83]. Both the numerator and the denominator are stored directly in SH (*not* as 3D histograms), and a procedure to calculate the correlation function directly from them (again, *not* involving any 3D histogram) has been presented [83]. An additional benefit of the method is that the covariances between all l, m components are explicitly taken into account. Unless otherwise noted, all further correlation functions presented in this work are represented using this method. We also recommend that experimental groups use this method.

As was the case for identical-particle femtoscopy, the SH representation turned out to have specific synergies with the nonidentical femtoscopic correlation analysis. The important femtoscopic information is contained in only two l, m components, while the other two can be used as additional cross-checks of experimental procedures. If one wishes to analyze the full 3D information, one needs to analyze only two more l, m components: the rest can be essentially neglected, as they should be consistent with 0 or they will not contain additional useful information.

We now investigate the important components of the SH decomposition and their sensitivity to femtoscopic information. We perform a simple calculation in which we assume the source to be a 3D Gaussian in an LCMS, having three different sizes R in three directions (out, side, and long). It also has a nonzero mean value μ_{out} in the out direction:

$$S(\mathbf{r}) = \exp\left(-\frac{(r_{\text{out}} - \mu_{\text{out}})^2}{R^2_{\text{out}}} - \frac{{r_{\text{side}}}^2}{R^2_{\text{side}}} - \frac{{r_{\text{long}}}^2}{R^2_{\text{long}}}\right). \quad (33)$$

With this source function we perform the integration, Eq. (15), to calculate the correlation function and present it in the SH representation. We expect that the main femtoscopic information is contained in the following components: C_0^0, $\Re C_1^1$, $\Re C_0^2$, and $\Re C_2^2$.

To study the sensitivity to the source size, we increase the overall size but keep the radius ratios the same. The results are plotted in Fig. 12. All components show some sensitivity, but C_0^0 is affected the most.

In the next step (shown in Fig. 13) we keep the source size the same, while we increase the emission asymmetry (μ_{out}). The main sensitivity is in the $\Re C_1^1$ component. More importantly, no asymmetry results in vanishing $\Re C_1^1$, while increasing the asymmetry increases the signal in

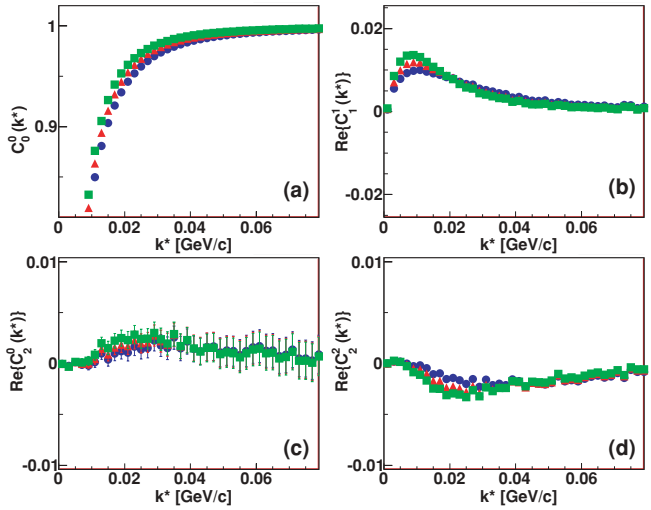

FIG. 12. (Color online) SH components of the correlation function for $R_{\mathrm{out}} = 8$ fm, $R_{\mathrm{side}} = R_{\mathrm{long}} = 4$ fm, and $\mu_{\mathrm{out}} = -4$ fm [(blue) circles], $R_{\mathrm{out}} = 10$ fm, $R_{\mathrm{side}} = R_{\mathrm{long}} = 5$ fm, and $\mu_{\mathrm{out}} = -5$ fm [(red) triangles], and $R_{\mathrm{out}} = 12$ fm, $R_{\mathrm{side}} = R_{\mathrm{long}} = 6$ fm, and $\mu_{\mathrm{out}} = -6$ fm [(green) squares].

$\Re C_1^1$ monotonically, approximately linearly. $\Re C_1^1$ is functionally equivalent to the out double-ratio. Obtaining quantitative as well as qualitative information about the asymmetry should be possible from the analysis of it (in correlation with at least C_0^0, where sensitivity is also seen, but to a lesser degree). In addition, from Eq. (30), we concluded that to maximize the significance of the asymmetry signal, one should integrate the correlation function with a weight equal to $\cos(\psi)$ [79]. Remarkably, the definition of $\Re C_1^1$ is essentially

$$\Re C_1^1(q) = N \int C(q, \cos(\theta_q), \phi_q) \sin(\theta_q) \cos(\phi_q) d\Omega_q, \quad (34)$$

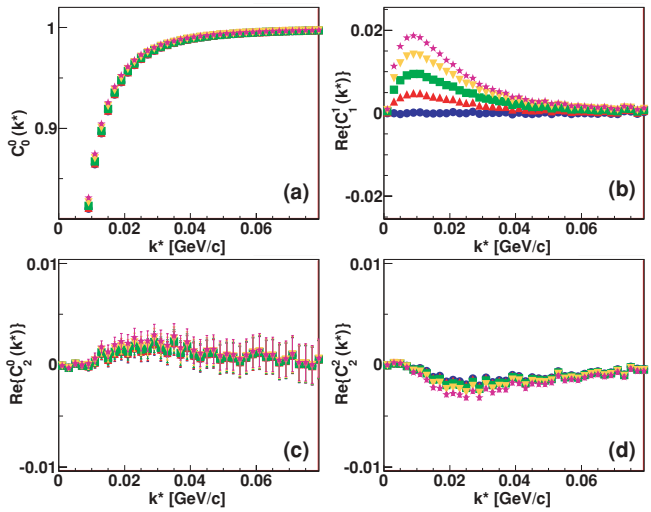

FIG. 13. (Color online) SH components of the correlation function for $R_{\mathrm{out}} = 10$ fm, $R_{\mathrm{side}} = R_{\mathrm{long}} = 6$ fm. Emission asymmetry μ_{out} is changed from 0 fm [(blue) circles] to -2 fm [(red) upward triangles], -4 fm [(green) squares], -6 fm [(yellow) downward triangles], and, finally, -8 fm [(violet) stars].

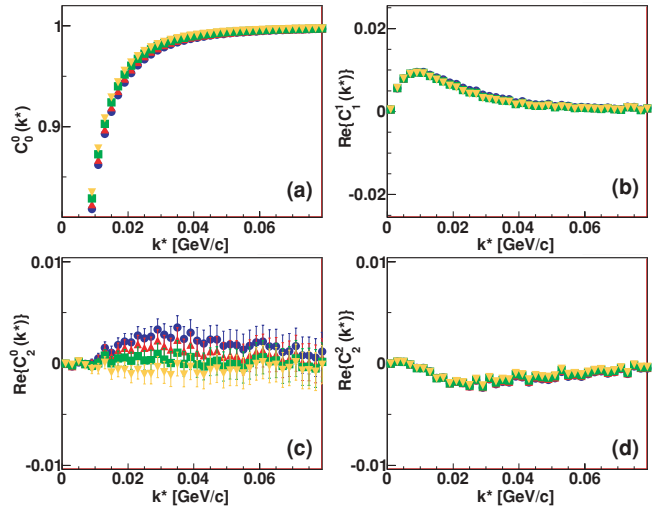

FIG. 14. (Color online) SH components of the correlation function for $R_{\mathrm{out}} = 10$ fm, $R_{\mathrm{side}} = 4$ fm, $\mu_{\mathrm{out}} = -4$ fm. R_{long} is changed from 4 fm [(blue) circles] to 6 fm [(red) upward triangles], 8 fm [(green) squares], and, finally, 10 fm [(yellow) downward triangles].

where N is the normalization factor, while θ_q and ϕ_q are the longitudinal and transverse components of the ψ angle. The $\Re C_1^1$ component happens to be the optimal way to maximize the *transverse* components of the asymmetry signal, owing to its $\cos(\phi_q)$ weight, while the $\Re C_1^0$ maximizes the longitudinal asymmetry signal, owing to its $\cos(\theta_q)$ weight:

$$\Re C_1^0(q) = N \int C(q, \cos(\theta_q), \phi_q) \cos(\theta_q) d\Omega_q. \quad (35)$$

Once again, it appears as if the SH were specifically designed for the femtoscopic correlation function representation.

Next, in Fig. 14 we keep the transverse source size and the asymmetry the same, while we change the R_{long} radius. Obviously we see a change in the C_0^0, which reflects the growth of the overall system size. But the most sensitive component is $\Re C_2^0$, which carries information about the ratio of the transverse to the longitudinal radii, owing to its $\cos^2(\theta_q)$ weighting.

Finally (see Fig. 15), we keep the sum of the transverse radii the same, but we change their ratio. The $\Re C_2^2$ component, with its $\cos^2(\phi_q)$ weighting, is the most sensitive to these changes, while the others remain practically constant.

The preceding calculations show that by analyzing just two components of the SH decomposition (C_0^0 and $\Re C_1^1$), one can already perform a meaningful femtoscopic analysis and determine the overall source size and emission asymmetry. Adding just two more components ($\Re C_2^0$ and $\Re C_2^2$), one can also determine source radii in all three directions, which would normally require a full analysis of a 3D correlation function. A full 3D analysis does require larger statistics than a 1D size + asymmetry one, as the sensitivity to the observables in the $l = 2$ components is smaller than in the $l = 0$ and $l = 1$ ones. One should stress that in the SH representation one is dealing with 200 data points (50 points per histogram, 4 components), versus the 625 000 bins in the 3D histogram representation. The huge savings in computation time and

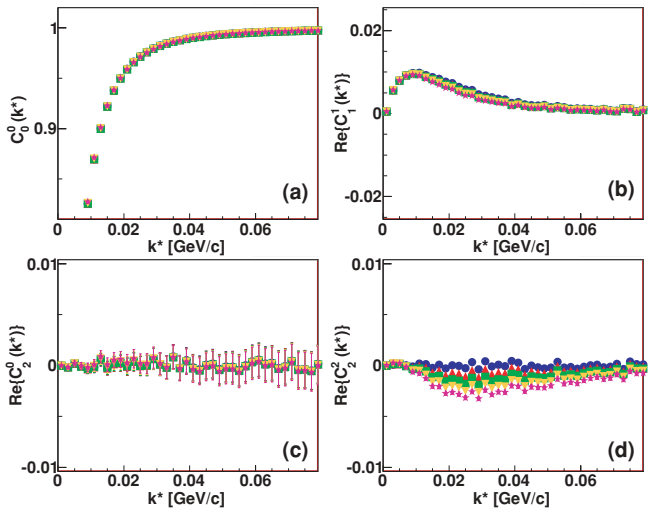

FIG. 15. (Color online) SH components of the correlation function for $R_{\text{long}} = 8$ fm, $\mu_{\text{out}} = -4$ fm. The transverse radius sum is kept constant: $R_{\text{out}} = 7$ fm, $R_{\text{side}} = 8$ fm [(blue) circles]; $R_{\text{out}} = 8$ fm, $R_{\text{side}} = 7$ fm [(red) upward triangles]; $R_{\text{out}} = 9$ fm, $R_{\text{side}} = 6$ fm [(green) squares]; $R_{\text{out}} = 10$ fm, $R_{\text{side}} = 5$ fm [(yellow) downward triangles]; and $R_{\text{out}} = 11$ fm, $R_{\text{side}} = 4$ fm [(violet) stars].

method complexity do not compromise the physics: one is able to obtain essentially the same femtoscopic information (three sizes and emission asymmetry). This means that the 3D representation is a particularly inefficient way of storing the femtoscopic information, while the SH one seems to be perfectly tailored for that task. We add that in all theoretical calculations that we have done, all the other components either were required to vanish from symmetry relations, were consistent with 0, or contained femtoscopic information that was already accessible via the four main components. In experiments, one should, in addition, look at the $\Re C_1^0$ (equivalent to the long double-ratio) and $\Im C_1^1$ (equivalent to the side double-ratio). The former is expected to show 0 asymmetry, and the latter is required to vanish for symmetry reasons, but their deviations from 0 may signal experimental reconstruction problems.

B. Extracting qualitative information

In the previous paragraph the sensitivity of the nonidentical particle correlation function to the source size and asymmetry was illustrated. Dependencies in Figs. 12–15 show that source size parameters influence all SH components at the same time, and it is not possible to analyze them separately. In identical-particle femtoscopy, obtaining Gaussian source size parameters is straightforward: the integral in Eq. (15) can be performed analytically if one assumes that $S(\mathbf{r})$ is a 3D Gaussian and does not depend on the pair momentum $\boldsymbol{K}$ (although the pair's transverse momentum K_T dependence can be recovered by K_T binning; rapidity binning is also possible). To take the Coulomb interaction into account, an approximate wave function is used in which the Coulomb part is factorized out and replaced with an averaged function that only depends on the magnitude of k^*. This procedure [84] enables one to write a simple analytic formula, which can be directly fitted to the 3D correlation function and provides femtoscopic radii.

In nonidentical-particle femtoscopy the Coulomb interaction is the source of the correlation, so it cannot be factorized out. Performing the integral in Eq. (15) analytically becomes impossible, especially when one needs to consider the strong interaction as well. The procedure must be carried out numerically. One starts with the same assumption as for identical-particle femtoscopy. The source is a 3D Gaussian, Eq. (33), where the additional modification allowing for a nonzero shift in the out direction is introduced. One then assumes a certain set of source parameters (R_{out}, R_{side}, R_{long}, μ_{out}) and calculates the corresponding correlation function, according to Eq. (15) and using the corresponding wave function, Eq. (16). As the source function is assumed to be momentum independent, one needs an input momentum distribution [the assumption of momentum independence of the source function is not required provided that the selected (p_T, y) is sufficiently narrow]. This can be achieved by, for example, taking particles' momenta from real pairs from data and assigning the separation $\mathbf{r}^*$ randomly generated from Eq. (33). The resulting "model" correlation function is compared to the "measured" one via a χ^2 test. The procedure is repeated for several sets of source parameters to find the one that fits the "data" best. This set is taken as the result of the fit. The procedure can be refined by ensuring that the model calculation is done for points that form a regular "mesh" in the parameters' space. In the simplest one-parameter fit, one obtains the fit value and error from the location of the χ^2 minimum on the parabola. When two independent parameters are fitted (the most common case for nonidentical correlations, where we usually fit overall radius R and emission asymmetry μ), one creates a 2D "mesh," to which one can fit a 2D parabola—obtaining the best-fit parameters and their error bars, as well as the covariance between them. An example of such an analysis is shown in Fig. 16. One can also employ a minimization package (e.g., Minuit) to perform the fitting process. The number of points in the coefficient

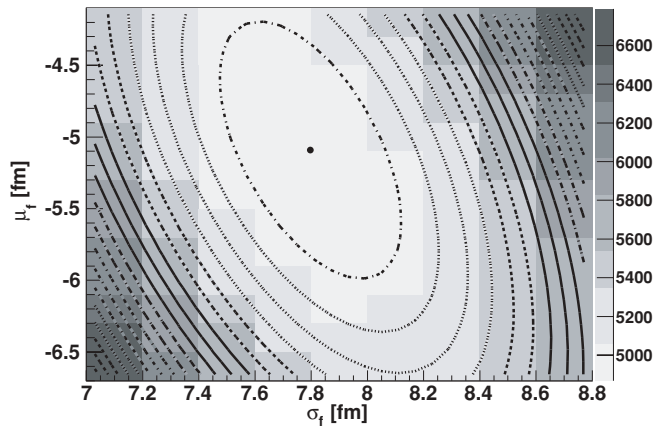

FIG. 16. An example of the 2D χ^2 map obtained by fitting a nonidentical-particle correlation function. The underlying colored histogram represents the "mesh" obtained in the fitting procedure. The lines represent a fitted 2D parabola. The filled circle represents the minimum of the parabola: the best-fit value.

function mesh can be kept at a minimum by using a simple linear or quadratic interpolation between points [10,35].

For the results presented in this work we used the software package CORRFIT to perform the numerical fitting procedure just described. It was developed for the analysis of nonidentical-particle correlations in the STAR experiment [39,85]. It allows for significant flexibility when choosing various parameters of the fitting process. For this work we have made the following choices. (1) The input data were correlation functions in SH representation. Only the C_0^0 and $\Re C_1^1$ components were fitted; the covariance between the two was taken into account. (2) The particular form of the S from Eq. (33) was taken, with the additional constraints that R_{side} was assumed to be equal to R_{out}, while $R_{\text{long}} = 1.3R_{\text{out}}$, following the identical-particle 3D femtoscopic results for pions from the RHIC [86]. Therefore, only two independent parameters were fitted: R_{out} and μ_{out}. (3) The input momentum distributions were taken from the STAR experiment, ensuring that the momentum acceptance was the same. (4) The standard package of R. Lednicky was used to calculate the pair weights [10,14]. The input theoretical correlation functions were calculated taking into account Coulomb interaction only. In this case, only the Coulomb part of the pair weight was calculated in the fitting procedure. (5) One had the possibility to introduce "pair purity" and momentum resolution corrections. Details on the purity correction are discussed later in this section. The momentum resolution correction was not necessary for model studies shown in this paper.

C. Influence of pair purity

For femtoscopic analysis one of the main experimental issues is the "purity" P of the analyzed pair sample, that is, the fraction of pairs in the sample that should be treated as "femtoscopically correlated." There are several reasons why a pair of particles should not be treated as correlated. From the experimental side, it may happen that one (or both) of the particles in the pair has been misidentified (this is why P is traditionally called purity). Another common scenario is when one of the particles is a product of a weak decay. In that case, it is the "parent" particle that should be treated as femtoscopically correlated, leading in some cases to rather complicated cases of "residual correlations," that is, feed-down of the femtoscopic correlation between parent particles into the daughters' correlation function. Recently, such cases have been studied in detail in baryon-baryon correlations [41,87]. However, in systems considered in this paper, containing a meson, residual correlations are smeared away by the decay momenta, so such pairs should be treated as "not femtoscopically correlated." These experimental components of P are clearly experiment dependent and it is up to the experiment to correct for such effects (or at least provide a realistic estimate of P). We do not address it further in this work.

However, another contribution to P remains, the estimate of which is model dependent. If one of the particles in the pair comes from a strongly decaying resonance that lives a very long time, for example, the ω meson, we may need to treat it as being not femtoscopically correlated. That is because the source of the correlation, the pair wave function Ψ, usually peaks at low r^* values, while at large values it produces no correlation. This can be dealt with in two ways. The first is to assume, in the data analysis, a source function that perfectly describes such long-range r^* tails. However, this is difficult to do, and it is very dependent on the model used to model such tails. The other solution is to treat the particles in the tails as not femtoscopically correlated—in other words, to provide a model estimate of the decrease in P coming from long-lived resonances. This is usually done by assuming that a source is a 3D sphere with a Gaussian profile and counting any pair that is outside this sphere as noncorrelated. We note that "non-Gaussian effects" have been seen in the identical-particle correlations in all RHIC experiments [86,88]. They have been attributed, at least in part, to long-lived resonances [53], and recently, new techniques have been proposed to analyze them in detail [89]. Such analyses are not yet possible in nonidentical-particle analysis, so we limit ourselves to the simple model estimation of P.

We characterize the overall purity of a pair sample by a percentage of pure pairs P. It can be (and in the experiment it usually is) a function of $\boldsymbol{k}^*$. Assuming that the "nonpure" pairs are not correlated, the correlation function can be trivially corrected for purity:

$$C_{\text{corrected}}(\boldsymbol{k}^*) = (C_{\text{measured}}(\boldsymbol{k}^*) - 1)/P(\boldsymbol{k}^*) + 1. \quad (36)$$

Employing formula (36) requires a precise knowledge of the fraction of correlated pairs P in the measured sample. Any uncertainty in its value will be a source of systematic error. In contrast to identical-particle femtoscopy, P cannot be easily inferred from the fit, independently of the source parameters σ and μ. By inspecting Fig. 10 and Eq. (36), one concludes that lowering the purity influences the correlation function in a way that is similar to the changes introduced by varying the source size. One can obtain a satisfactory fit to the correlation function by adjusting either one of these parameters, so treating them both as free makes them highly correlated. While possible, the independent determination of σ and P requires significant statistics and very good control of the nonfemtoscopic background [10,35].

Usually, the practical solution is to come up with the best estimate of P by other means (both experimental and theoretical) and fix its value for the fitting. By performing the procedure for several fixed values of P, within the reasonable uncertainty range, one obtains the systematic error in the fit values coming from the purity estimate. As an example, in Fig. 17 we show how the fit values for the same input correlation function change as one adjusts the fixed pair purity P. Within the reasonable range of P variations of the order of 20%, the dependence of σ and μ on P is monotonic and noticeable. We expect that the purity estimate will be the major source of the systematic error. We address the theoretical part of the estimates of pair purity in Sec. VI B.

D. Influence of the momentum resolution

The momentum resolution will influence the femtoscopic correlation function in a well-defined way. Because reconstructed momenta will differ from the true ones, the correlation effect (visible as either a "peak" or a "depression" at low k^*) will be reduced. The Coulomb correlation is rather sharp at a

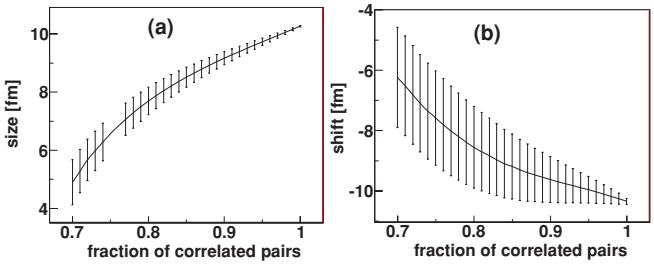

FIG. 17. (Color online) Values of the correlation function fit—size (a) and shift (b)—as a function of a predefined fraction of primary pairs.

low relative momentum, so one expects the small k^* points to be influenced the most. The double-ratio will be affected as well. One can study the influence of the momentum resolution by performing a theoretical calculation in the following way. One calculates C according to Eq. (32) but calculates two sets of relative momenta k^* for each pair. The first one, k^*_{true}, is used to calculate Ψ, and the second one, k^*_{smeared}, is used to determine the correlation function bin in which the pair is stored. The second set is calculated by smearing the particles' momenta with the parametrization of the momentum resolution obtained from the experiment. By comparing the "unsmeared" and "smeared" correlation functions, one can judge the importance of the momentum resolution effect. One can also employ the same technique when calculating the "theoretical" correlation functions during the fitting procedure described in Sec. V B. In this way the fitting procedure automatically corrects for the momentum resolution. The precise determination of the momentum resolution parameters is very dependent on the experimental features. We do not discuss it further in this work (see, e.g., Ref. [35]).

VI. SYSTEMATIC CHECKS OF THE METHOD

In the previous sections we have made qualitative claims that analysis of the nonidentical-particle correlations should enable estimation of the source size and emission asymmetry for pions, kaons, and protons emitted in the heavy-ion collision. In this section we aim to show the quantitative checks of the method. We focus on answering two questions: Can the method reliably and quantitatively recover the source size and emission asymmetry? And if yes, what systematic uncertainties in this estimation come from the method itself?

We emphasize that in this section we focus only on the technical aspect of the nonidentical-particle correlations method. So, the THERMINATOR calculations are used only as "test samples."

A. Details of the procedure

We chose the following procedure: we simulate heavy-ion Au + Au collisions with the THERMINATOR model. We do it for six centrality bins: 0–5%, 5%–10%, 10%–20%, 20%–30%, 30%–40%, and 40%–50%. We calculate the full set of nonidentical correlation functions: same- and opposite-sign pion-kaon, same- and opposite-sign pion-proton, and same-sign kaon-proton for these centralities, producing $6 \times 5 = 30$ independent correlation functions. Then we proceed to treat these functions as if they were experimental ones: applying the purity correction and fitting them with the CORRFIT software. In the end we compare the input values from the model with the fit results and see if they match.

We simulated 50 000 events for each centrality. The parameters of the model were the same as those used in Refs. [26] and [50], which are known to reproduce both single-particle spectra and overall femtoscopic sizes from identical-particle correlations. The correlation functions were calculated by combining particles from these events into pairs and employing Eq. (32). The SH representation of the correlation function was used. Then each function was fitted with the CORRFIT program, assuming that the two-particle source is a 3D Gaussian in an LCMS, according to Eq. (33). The sideward and longitudinal sizes of the source were fixed to be equal to R_{out} and $1.3R_{\text{out}}$, respectively, according to the results obtained for identical pions. In this way the fitting procedure had only two parameters: overall size R_{out} and emission asymmetry μ_{out}. We note that while the full 3D analysis, with R_{side} and R_{long} as independent free parameters of the fit, is possible in principle, we do not discuss it in this paper, as we consider it less interesting: it would provide 3D information about the source, but with a much lower precision than the 3D identical pion analysis. Instead, we choose to focus on asymmetry, which is a unique observable accessible only via nonidentical particle femtoscopy.

B. Characterizing model input

Let us inspect a typical two-particle emission function S_{AB} coming from the THERMINATOR model, shown in Fig. 18. The distributions in the out, side, and long directions show different behavior. Only the side one is well described by a Gaussian; attempts to fit the out and long distributions by Gaussians are shown as dashed lines. The long-direction distribution can be

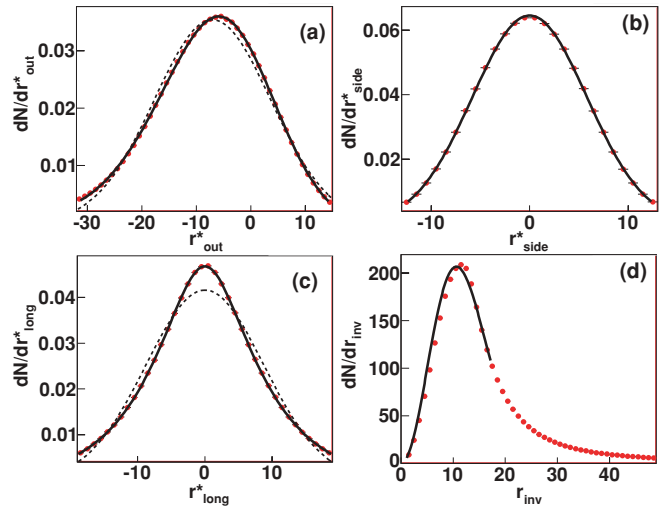

FIG. 18. (Color online) Two-particle emission function for pion-kaon pairs at centrality 10%–20%. (a) r^*_{out}; (b) r^*_{side}; (c) r^*_{long}; (d) r_{inv}. Lines are fits to the distributions; see text for details.

described by an exponential hyperbola function:

$$f_{\mathrm{EH}} = \exp\left(-\sqrt{\frac{r_{\mathrm{long}}^{*\,2}}{\sigma_{\mathrm{long}}^2} + \alpha^2}\right), \tag{37}$$

where σ and α are parameters. For description of the out-direction distribution, one needs an asymmetric exponential hyperbola:

$$f_{\mathrm{EH}}^{\mathrm{as}} = \exp\left(-\sqrt{\frac{(r_{\mathrm{out}}^* - \mu_{\mathrm{out}})^2}{\sigma_{\mathrm{out}}^2} + \alpha^2}\right)(1 + \zeta(r_{\mathrm{out}}^* - \mu_{\mathrm{out}})), \tag{38}$$

where $\sigma_{\mathrm{out}}, \mu_{\mathrm{out}}, \alpha_{\mathrm{out}}$, and ζ are parameters. We have confirmed that these functional forms are general; that is, one is able to fit them to the emission functions at all centralities and for all pair types. In contrast, the fitting procedure that we described in the previous section assumes a proper Gaussian source distribution. Therefore, one needs to find a suitable variable that will enable comparison between the model input, which is non-Gaussian, and the fit output, which is postulated to be a Gaussian. In principle, one can think of removing the Gaussian assumption and actually using the functional forms mentioned previously for the fitting. This is certainly possible, from the point of view of both the technique and the software tools. However, it poses two potential problems. First, while the functional forms are able to fit the THERMINATOR data very well, there is no reason to assume that this will be the case for other models. So, by choosing these particular forms, one would introduce a strong model dependence. Moreover, it is not known how the parameters of these functions could be compared to the Gaussian radii from identical-particle femtoscopy. In this work we access the overall directionally averaged size of the system only, so the details of the source function dependence in the three directions separately will be lost. In this work we decided to use the Gaussian assumption, having in mind that it may introduce systematic effects, when comparing the fit values to input two-particle distributions.

We are then presented with the following situation: the "experimental" fit procedure produces the direction-averaged source size R and the emission asymmetry in the out direction μ_{out}. In contrast, to fully describe the theoretical model input, one needs the following parameters: σ_{out}, α_{out}, ζ, μ_{out}, σ_{side}, σ_{long}, and α_{long}. To compare the two, one needs to find common variables that can be compared and that will tell whether our experimental fit reproduces the "model input."

In traditional HBT, one compares 1D femtoscopic radii, defined as the σ of a 1D Gaussian approximation of the single-particle emission function (usually in the PRF). We wish to define an analogous variable for nonidentical study, but defined in an LCMS to facilitate the comparisons to the 3D identical-particle interferometry results. The task is complicated by the fact that neither the model input nor the experimental fit produces a source that is a perfect Gaussian. Nevertheless, one can plot the source distribution dN/dr in both cases. Then one fits the distribution with the Gaussian formula, multiplied by the proper Jacobian:

$$f_G(r) \approx \exp\left(-\frac{r^2}{2R_{\mathrm{av}}^L}\right) r^2. \tag{39}$$

As discussed later, one must restrict the range of this fit to low-r values, as these are the ones that contribute to the femtoscopic effect. The contributions from the large-r part of the source must be dealt with separately. Figure 18(d) shows an example of the model r_{inv} distribution; the line is a fit according to Eq. (39), done in the range of 0–20 fm. Because both the r_{out} and the r_{long} distributions are manifestly non-Gaussian, so is the r_{inv} distribution.[4] Therefore, the fitted $R_{\mathrm{av}}^{\mathrm{input}}$ characterizes only the general size of the system. The same fitting procedure can be applied to the r_{inv} distribution produced by the experimental fit, producing the $R_{\mathrm{av}}^{\mathrm{fit}}$ "experimental" value. For a more detailed discussion of the approximate relations between 1D and 3D source size parameters and the relations between values in the PRF and those in the LCMS, as well as a more detailed description of estimating R_{av}, we refer the reader to the Appendix.

One also needs to define what the "emission asymmetry" μ_{out} means in the case of the model. One can come up with several definitions: (a) the "mean" of the r_{out}^* distribution, (b) the "mean" of the r_{out}^* distribution, but taking into account only parts of the distribution near the peak (neglecting the long-range tail), and (c) the position of the maximum in the r_{out}^* distribution. All three are correlated, but definition a shows a high sensitivity to long-range tails and therefore is not well defined. Of the other two, definition b should be exactly the same as $\langle r_{\mathrm{out}}^* \rangle$, which is the value used in the theoretical formalism, while the relation of definition c to $\langle r_{\mathrm{out}}^* \rangle$ is less straightforward. So, we chose to use definition b.

In Fig. 19 a comparison between "input" and "fitted" radii is shown, for all considered pairs, for both primordial and all particles. A clear correlation is seen between the two. However, most of the results do not lie on the "perfect" $x = y$ line. Within each pair system the correlation is clear and monotonic. Moreover, the deviations from the perfect curve seem to be a systematic shift, similar for all points of the same pair type. The shift from perfect values for a given pair type is seen both for the R_{inv} and the μ_{out} variables.

One obvious candidate for the explanation of this shift is the pair purity P. The fit procedure assumes that *all* the pairs in the source come from the region with a Gaussian density profile. In contrast, a realistic model, such as THERMINATOR, clearly shows that there are significant non-Gaussian long-range tails in the separation distributions; this is illustrated in Fig. 20. One can perform a simple calculation. Take the model radius R_{av}^L obtained from fitting the model separation distribution with Eq. (39); by integrating this distribution, one obtains the number of pairs N_G within the Gaussian core of the source. N_G is then the area below the fit curve in Fig. 20(d). This can be compared to the total number of pairs N_A obtained by simply counting the number of model pairs or, in other words, the area

[4] It can be shown that r_{inv} distribution is a Gaussian only if all three r_{out}, r_{side} and r_{long} are Gaussians and additionally all three have the same width.

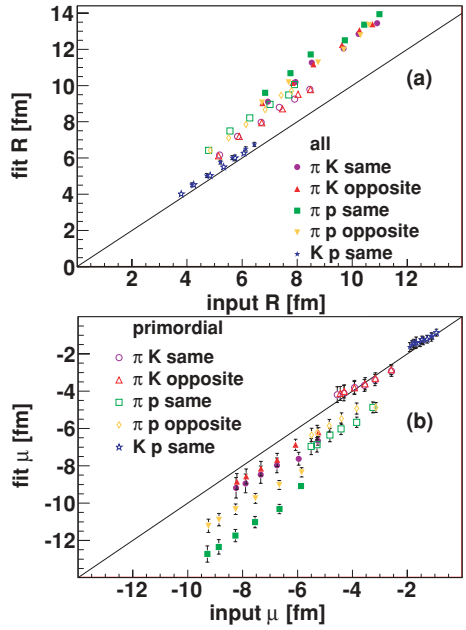

FIG. 19. (Color online) Correlation of input values obtained from the model and fit values. (a) Overall system size; (b) emission asymmetry in the out direction. Open represent calculations for primary particles only; filled symbols, for all particles. Circles (violet) are same-sign pion-kaon pairs; upward triangles (red), opposite-sign pion-kaon pairs; squares (green), same-sign pion-proton pairs; downward triangles, opposite-sign pion-proton pairs; stars (blue), same-sign kaon-proton pairs.

below the points in Fig. 20(d). The value $f_{\mathrm{FC}} = N_G/N_A$ is the number of "femtoscopically correlated" pairs and should be simply treated as purity in the sense discussed in Sec. V C. One needs to correct for these "non-Gaussian" effects. To do that, one calculates f_{FC} and then treats it as a fixed parameter

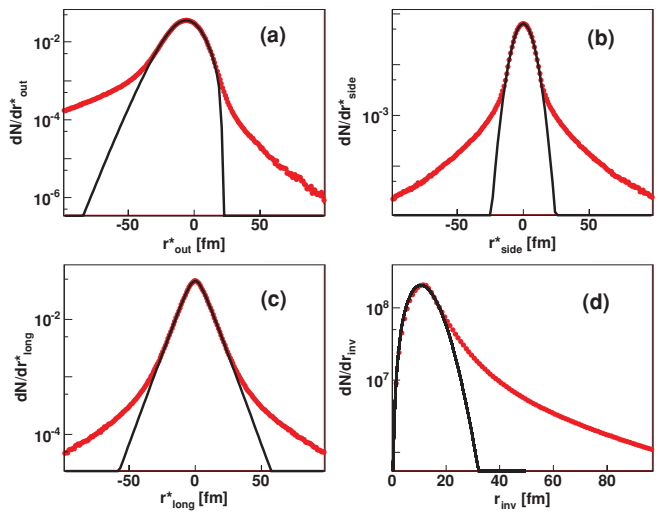

FIG. 20. (Color online) An illustration of the long-range tails produced by THERMINATOR. Points: separation distributions for pion-kaon pairs: (a) r_{out}, (b) r_{side}, (c) r_{long}, and (d) r_{inv}. Lines are fits to the region near the peak, using the functional forms: $f_{\mathrm{EH}}^{\mathrm{as}}$ for out, Gaussian for side, f_{EH} for long, and f_G for inv.

TABLE V. Estimate of the theoretical purity P for all pair types, versus centrality. See text for details.

	P, at c (%)					
	0–5	5–10	10–20	20–30	30–40	4–50
πK	0.83	0.82	0.80	0.76	0.73	0.70
πp	0.80	0.79	0.77	0.75	0.73	0.71
Kp	0.96	0.95	0.95	0.94	0.93	0.93

in the fitting process. Note that the f_{FC} estimation procedure, by design, takes into account two effects, which cannot be easily disentangled: the pairs in the long-range tails and the fact that the shape of the core system is not a Gaussian in a 1D representation. We have performed the estimation based on the input model pair separation distributions and find that f_{FC} depends on both the pair type and centrality. The exact values are listed in Table V. These values are obviously model dependent and are strongly influenced by the size of the long-range tails in the separation distributions. It is well known that the source of such tails is, to a large degree, particles coming from strongly decaying resonances. It is therefore important to use a model like THERMINATOR, which fully includes all known resonance propagation and decay, to determine purity. A clear trend exists for all pair types: the f_{FC} get smaller as collisions get more peripheral. The long-range resonance tails and non-Gaussian effects get relatively more important as one moves away from central collisions.

The experimental fits have been redone, this time with the purity fixed to the listed f_{FC} values. The results are shown in Fig. 21. All results now lie close to the perfect $x = y$ line within the statistical error. This shows that, having in mind the caveat mentioned previously, the analysis technique is able to produce reliable results, and the results of the experimental

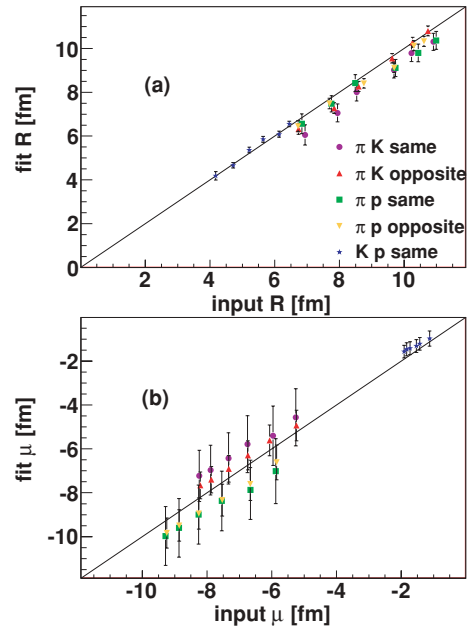

FIG. 21. (Color online) Same as Fig. 19, but the fit procedure was done with adjusted purity values (see text for details).

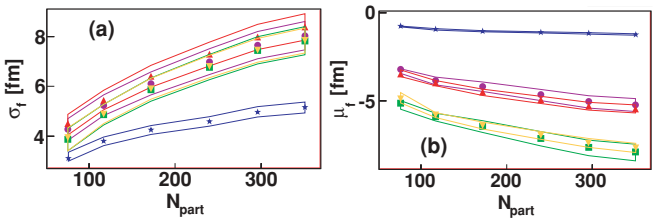

FIG. 22. (Color online) Fitted parameters for all pair types, versus centrality. (a) System size (σ); (b) emission asymmetry (μ). Colors and symbols are the same as in Fig. 19. The bands represent the change in the fit parameters as the fixed purity P is changed by ± 0.05 for pion-kaon and pion-proton pairs and by ± 0.03 for kaon-proton pairs.

fitting procedure do indeed provide valuable information about the particle-emitting source. In particular, both the direction-averaged size of the source and the emission asymmetry can be reliably recovered.

The inherent uncertainty in the determination of f_{FC} is the source of the systematic error introduced by the method itself. In Fig. 22 we show how the fit value changes when the purity is varied within a reasonable range (± 0.05 for pion-kaon and pion-proton and ± 0.03 for kaon-proton). This results in the following systematic uncertainties in the obtained values: for same-sign pion-kaon, 7% on σ and 7% on μ; for opposite-sign pion-kaon, 7% on σ and 4% on μ; for same-sign pion-proton, 8% on σ and 6% on μ; for opposite-sign pion-proton, 7% on σ and 4% on μ; and for same-sign kaon-proton, 5% on σ and 4% on μ.

We note that the f_{FC} estimation presented here is specific to THERMINATOR and represents the uncertainty within this model itself. In addition, the absolute value as well as an estimated uncertainty of f_{FC} can be different in other models, for example, in rescattering codes. The total systematic uncertainty of the experimental measurement should take this model dependence into account. In addition, the experimental purity, that is, the efficiency of particle identification, will also contribute to the same uncertainty.

VII. RESULTS OF "EXPERIMENTAL-LIKE" ANALYSIS

In Sec. V we described, in detail, the experimental procedure to analyze nonidentical-particle correlations. For the model analysis of the THERMINATOR output, we used the complete two-particle method for calculating the correlation function and obtained the pion-kaon, pion-proton, and kaon-proton correlation functions. They are, from the point of view of a formalism and our analysis methods, identical to the correlation functions that one might obtain in the experiment. We calculated sets of 1D histograms that correspond to these functions represented in SH. We neglected the strong interaction component of the pair wave function for simplicity and speed of calculation. Then we switched this effect off in the fitting procedure as well. Obviously, when fitting the true experimental functions, one will use the full pair wave-function calculation. The strong interaction effect is known to be small compared to the Coulomb for the pairs of interest, so we do not expect any systematic effect on the fit values coming from this simplification. In addition, in the real experimental correlation function, one expects some nonfemtoscopic effects in addition to the pure femtoscopic one. These need to be dealt with on a case-by-case basis, as they will strongly depend on experimental conditions. For this discussion we assume that any such effects can be identified and that the experimental correlation function can be properly corrected, so that only the femtoscopic effect remains.

We proceeded to treat the calculated correlation functions as if they were coming from the experiment. No other information, except for the pair purities, is used in the procedure. For purity correction we used the values listed in Table V, as we would have done in the real data analysis. The goal of the exercise is to confirm that the obtained "experimental fit values" actually correspond to the true values, shown in the previous section and obtained directly from the emission functions. The example correlation functions together with the fitted "model" ones are shown in Fig. 23. For pion-kaon and pion-proton pairs, one can see a positive correlation effect for opposite-sign pairs and a negative one for same-sign pairs. The $\Re C_1^1$ components also show a mirror effect. For kaon-proton pairs the correlation effect starts at a larger k^* (is wider) and is more pronounced, as expected from the lower Bohr radius for this pair. The lines show the functions fitted with the CORRFIT program.

The fitting described in Sec. IV assumes that the source is a 3D Gaussian in an LCMS. The direct output of the fitting procedure is the size of the system in the out direction σ^f and the emission asymmetry μ^f in that direction. From these values one can calculate, via the relations specified in the Appendix, all the other source size characteristics. In the fitting procedure each pair is treated individually, so its velocity is known. One can therefore directly determine the direction-averaged source size in the PRF: there is no need

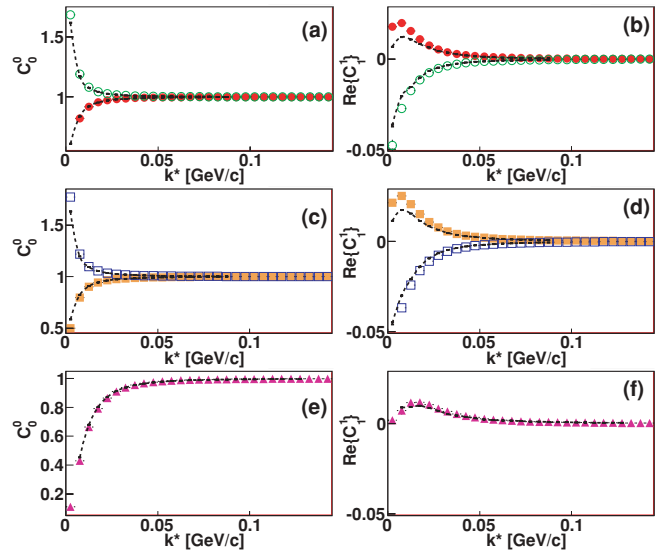

FIG. 23. (Color online) Example of the correlation functions calculated with the THERMINATOR + LHYQUID model for central Au + Au collisions. (a, c, e) C_0^0 components; (b, d, f) $\Re C_1^1$. Filled circles are same-sign pion-kaon pairs; open circles, opposite-sign pion-kaon pairs; filled squares, same-sign pion-proton pairs; open squares, opposite-sign pion-proton pairs; triangles, same-sign kaon-proton pairs. Lines show the best-fit "model" correlation functions.

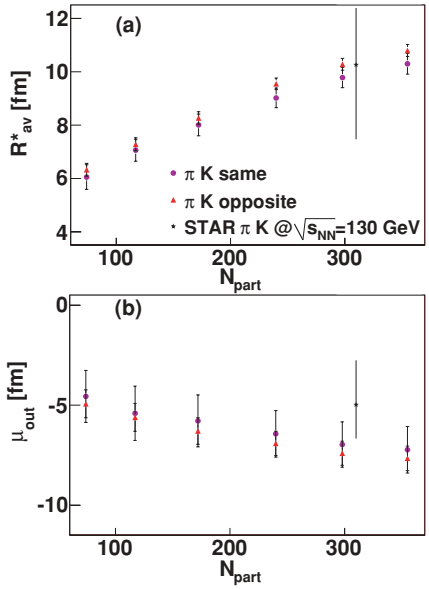

FIG. 24. (Color online) Source parameters in the PRF for pion-kaon pairs obtained from the "experimental" fitting procedure. (a) Source size; (b) emission asymmetry. Circles represent same-sign pairs; triangles, opposite-sign pairs. The star is a STAR measurement [39] at $\sqrt{s_{NN}} = 130$ GeV; the line represents statistical + systematic error (see text for details).

to use the averaged pair velocity in transformation from the LCMS to the PRF, as in Eq. (A15). In Figs. 24–26 we plot this directionally averaged radius in the PRF, $R^*_{\rm av}$. One must choose one of the three equivalent values, σ_f, $R^L_{\rm av}$, and $R^*_{\rm av}$, for presentation of the results. When we present the results of our calculations, we choose $R^*_{\rm av}$, as it is more natural than σ_f

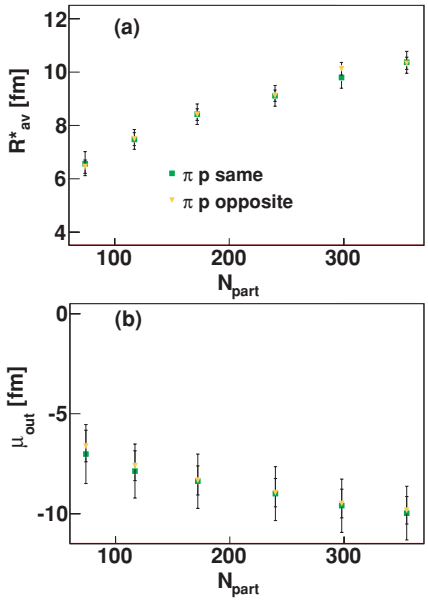

FIG. 25. (Color online) Source parameters in PRF for pion-proton pairs obtained from the "experimental" fitting procedure. (a) Source size; (b): emission asymmetry. Squares represent same-sign pairs; triangles, opposite-sign pairs.

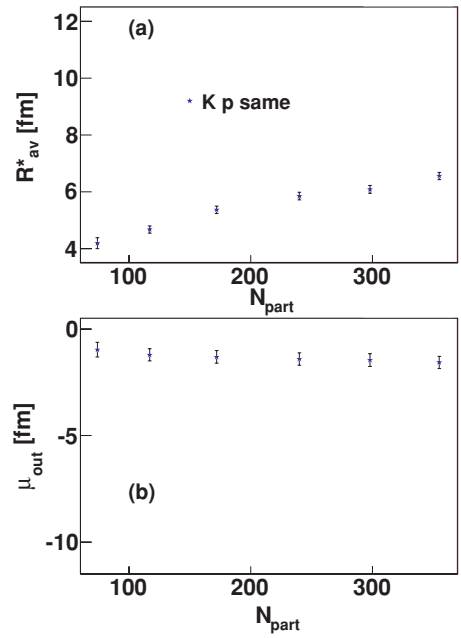

FIG. 26. (Color online) Source parameters in the PRF for kaon-proton pairs obtained from the "experimental" fitting procedure. (a) Source size; (b) emission asymmetry.

(which requires the knowledge of other direction multipliers to be meaningful) and describes the emission function in the PRF, so there is no need for the assumptions required in the LCMS-to-PRF transformation. In contrast, the 3D identical-particle femtoscopy analysis produces source sizes directly in the LCMS, so if we want to compare to these results, we will use $R^L_{\rm av}$.

In Fig. 24 we show the experimental-like fit results $R^*_{\rm av}$ for pion-kaon pairs. This should be compared to the "true" values in Fig. 6. The correlation between "true" and "fitted" values is also shown directly in Fig. 21. We can see that even with all the assumptions and simplifications that are used in the fitting procedure, one is able to recover the true system size. The accuracy for same-sign pion-kaon function is 8%; for opposite signs it is 5%, with the largest deviation of 10%. These are comparable to the statistical error of the fit. For the asymmetry, the "input" and "fit" values were identical within 10%. All results were in agreement within the statistical error of the fit.

A single measurement is available for the pion-kaon system at the RHIC, made by STAR at $\sqrt{s_{NN}} = 130$ GeV [39]. To compare it with the values presented in Fig. 24, we needed to account for two effects. The measurement was corrected for a fraction of *nonprimary* particles (particles not coming from the primary vertex), which is an experimental correction. But it was not corrected for *noncorrelated primary pairs*, a correction that we have described in this work. Taking the dependency in Fig. 17 as a guideline and the purity estimate of 0.85 for a pion-kaon pair in central Au + Au, we have scaled the reported system size and asymmetry accordingly. Moreover, the fitting performed in Eq. [39] assumed a specific shape (size equal in the out, side, and long directions in the PRF), from which we recalculated $R^*_{\rm av}$, to be compared with results in this work.

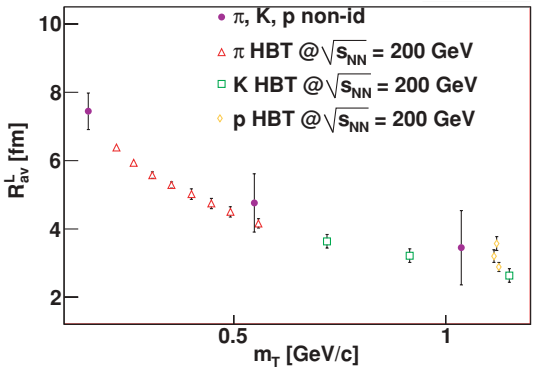

FIG. 27. (Color online) Comparison of overall size obtained from the nonidentical-particle calculation with the RHIC data for central Au + Au collisions at 200 GeV/c. Filled circles represent (from left to right) single-particle pion, kaon, and proton radii inferred from nonidentical simulations (centrality 5%–10%); open triangles are pion radii from STAR [90] (centrality 0–5%); open squares are pion radii from PHENIX [91] (centrality 0–30%); and open diamonds are proton results from STAR [87] (centrality 0–10%).

The measurement was done at a colliding energy different from the one considered in this work, so we plot the result at a corresponding N_{part}. One can see that the system size is in perfect agreement with the model predictions in this work; the asymmetry seems to be slightly smaller than the prediction, but in agreement within the statistical + systematic error.

In Fig. 25 the same results are shown for pion-proton pairs. The accuracy of the system size determination is 5%, comparable to the statistical fit error. The asymmetry is reproduced with poorer quality, with discrepancies of up to 12%, comparable to the statistical error.

In Fig. 26 the results are shown for kaon-proton pairs. The system size determination is good: 3%, better than the statistical fit error. The asymmetry is reproduced with discrepancies of up to 15%; however, because the absolute values are small (compared to the pion-kaon and pion-proton case), the absolute value of the difference is comparable to the systematic error of the fit. We conclude that the system size and the emission asymmetry can be reliably recovered, with the systematic error owing to the procedure itself less than 10%. However, one must correctly determine the systematic error owing to the pair purity estimation as well. We note that tests of the method have been performed for the THERMINATOR model only, so they are not necessarily general. However, the tests were done for many centralities (system sizes) and pair types, and the method was found to work in all cases, so we have some confidence that it should work for other models as well. One possibility for further studies is to perform similar tests with a model that introduces particle rescatterings.

One would also like to compare the results of nonidentical-particle correlations with the wealth of data coming from femtoscopic analysis at the RHIC. This presents a complication, as the identical-particle femtoscopy is usually presented in 3D form as single-particle "HBT radii" R_{out}, R_{side}, and R_{long}, while for analysis in this work, we have the averaged two-particle source size σ^f and emission asymmetry μ^f_{out} only. From its definition we conclude that, for example, $\sigma^f_{\pi K}$

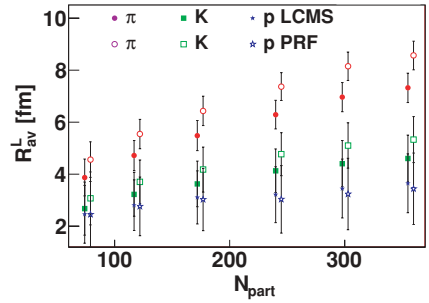

FIG. 28. (Color online) Single-particle source sizes inferred from the nonidentical simulations versus centrality. Filled symbols represent LCMS sizes; open symbols (shifted for clarity), for PRF sizes. Circles denote pions; squares, kaons; stars, protons.

should correspond to the variance of convolution of two Gaussians: one with variance of R_{out} for pions and the other with variance of R_{out} for kaons at the same velocity. Both the identical-particle R's and the nonidentical σ^f are defined in the LCMS. Again, we refer the reader to the Appendix for explicit relations between the two. From the input data (either R_{out}, R_{side}, and R_{long} in the LCMS for identical particles or σ_f and μ_f for nonidentical particles), we calculate the directionally averaged source size R^L_{av}. By comparing these values, defined in the LCMS, as opposed to the R_{inv} defined in the PRF, we avoid the unnecessary approximation coming from the determination of the averaged pair velocity, needed for the determination of $\langle\gamma\rangle$. This comparison is made in Fig. 27, where data from most central Au + Au collisions are shown. The open symbols are experimental data for pions, kaons, and protons. The filled symbols are single-particle source sizes inferred from fits to the nonidentical-particle correlation functions calculated with THERMINATOR. One can see a very good agreement between the model prediction and the data. All data points follow the "m_T scaling" trend predicted by hydrodynamics. A direct comparison of nonidentical-particle sizes and asymmetries between model and data would be an even better test. However, we stress that such comparisons can only be made provided that other observables related to source dynamics, such as, for example, particle spectra, elliptic flow, and identical-particle femtoscopy, are reproduced in the model. These tests have been performed for THERMINATOR in earlier works [26,50].

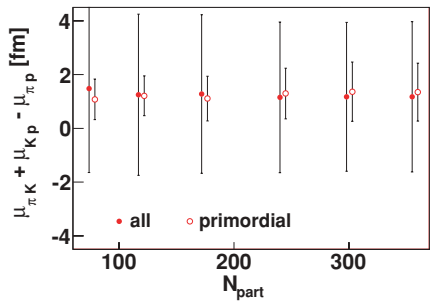

FIG. 29. (Color online) Emission asymmetry consistency cross-check versus centrality. Filled circles represent all particles; open circles (shifted for clarity), primordial particles only.

We have calculated the single-particle source sizes for all centralities and plotted them in Fig. 28. An ordering of source sizes with particle mass is seen, as expected, as well as an increase in the overall source size with N_{part}. Sizes for the PRF are larger, as the out radius is scaled by the $\langle \gamma_t \rangle$ factor.

As a final cross-check we show in Fig. 29 that the emission asymmetries do add up to 0 within the systematic error of the measurement.

VIII. CONCLUSIONS

The THERMINATOR + LHYQUID model has been briefly introduced and shown to have a unique set of features: hydrodynamic expansion and inclusion of resonance propagation and decay for all known particle types. Both features are important for nonidentical-particle femtoscopy. Simulations with this model provided predictions for emission asymmetries between particles of different masses and validated the analysis methods of nonidentical-particle femtoscopy.

We have emphasized the importance of the emission asymmetry measurement and provided predictions for RHIC energies. We showed that "emission asymmetry," or the nonzero difference in the mean emission points of particles of the same velocity but different masses, is predicted to arise in hydrodynamical calculations. It was shown to be intimately related with the collective behavior of matter and to be a direct consequence of the x-p correlations. It is the most direct and unambiguous femtoscopic signal of such behavior and provides an independent strong constraint on models aiming to describe the space-time evolution of a heavy-ion collision. Specific predictions, both qualitative and quantitative, have been given for such asymmetries, for all the considered pair types (pion-kaon, pion-proton, kaon-proton). It was shown that the lighter particle is always emitted closer to the center of the source, giving a negative emission asymmetry μ_{out} in the out direction. Predictions of the size of the source, including the dependence on centrality, have also been given, which were cross-checked with the more precise results from identical-particle femtoscopy.

The influence of strongly decaying resonances on emission asymmetries has also been studied in detail. It was shown that, because of a specific combination of decay kinematics properties for particles of different masses, the emission asymmetry produced by an earlier hydrodynamic stage is further magnified. At the same time the resonance decay process alone produces emission asymmetry an order of magnitude smaller than the x-p correlation, so it cannot be used as an alternative explanation of the phenomenon.

We have presented, in some detail, the theoretical basis and some technical aspects of nonidentical-particle femtoscopy, to be used in ultrarelativistic heavy-ion collisions. In particular, it was shown how to access the "emission asymmetry," a piece of femtoscopic information that can only be accessed via this type of analysis. It was pointed out that SH representation of the correlation function has useful synergies with the analysis; the use of this representation is strongly advocated. Important corrections to the correlation function were identified, namely, pair purity and momentum resolution, and experimentalist recipes were given for applying them to real data. Extracting femtoscopic information from the nonidentical-particle correlation function requires a numerical fitting procedure. It was described in detail and implemented as a computer code. It was also shown that, after application of the proper purity correction, the fit procedure was able to recover the "true" model input values, which was an important validation of the method.

An estimate of the "fraction of correlated pairs," coming from the significant non-Gaussian shape and long-range tails in the pair separation distributions, has been obtained, based on the THERMINATOR simulation. The value can be an input to an experimental analysis of RHIC data, however, one must keep in mind that it is model dependent. The systematic error coming from this theoretical estimate was also given.

Finally, the "experimentalist" analysis procedure, described in the paper, has been applied to the correlation functions obtained from the model calculations. It was shown that the method reliably recovers the input model values in realistic conditions. Internal consistency cross-checks were proposed and tested. A way to compare results of nonidentical- particle femtoscopy and femtoscopic sizes from identical-particle analysis has been presented; the THERMINATOR predictions were shown to be in agreement with available identical-particle HBT radius results from the RHIC.

ACKNOWLEDGMENTS

I would like to thank Richard Lednicky, Wojciech Florkowski, and Yiota Foka for comments and very helpful discussions.

APPENDIX A: EMISSION FUNCTION MEASURES

In femtoscopy one considers pairs of particles. Of particular interest are observables related to their relative separation $\boldsymbol{r}$. We refer the reader to the beginning of Sec. III for the description of symbol conventions, the reference system, and the relevant reference frames. The transition from the LCMS to the PRF is simply the boost along the outward direction, with the transverse velocity of the pair β_t:

$$\begin{aligned} r^*_{\text{out}} &= \gamma_t \left(r_{\text{out}} - \beta_t \Delta t\right), \\ r^*_{\text{side}} &= r_{\text{side}}, \\ r^*_{\text{long}} &= r_{\text{long}}, \\ \Delta t^* &= \gamma_t \left(\Delta t - \beta_t r_{\text{out}}\right). \end{aligned} \tag{A1}$$

However, in our calculation we always use the equal-time approximation, which means that we neglect the time difference Δt^* in the PRF. From the components we also calculate the length of the relative separation vector:

$$r^* \equiv r_{\text{inv}} = \sqrt{{r^*_{\text{out}}}^2 + {r^*_{\text{side}}}^2 + {r^*_{\text{long}}}^2}. \tag{A2}$$

The two-particle emission function is, from a mathematical point of view, any function of the separation four-vector, $S(\Delta x)$, where $\Delta x = \{\Delta t, r\}$ can be expressed in any reference frame. In femtoscopy we use specific functional forms of S,

which are characterized by parameters. One must keep in mind that even though the relation between *relative separation* $\boldsymbol{r}$ values in the LCMS and those in the PRF is given by a simple equation, Eq. (A1), the relations between *source function parameters* (R's and μ) in these reference frames may not be as simple. Moreover, even if there exists a simple parametrization of the source in 3D variables ($r_{\rm out}, r_{\rm side}, r_{\rm long}$), this does not mean that this source distribution expressed in the magnitude of the relative separation r will also have a simple parametric form. The aim of this Appendix is to derive relations between commonly used source function parameters, defined in various reference frames, as well as between 3D and 1D representation parameters. Similar considerations for different source parametrizations have been done in the past [92].

We must also repeat the description of Eq. (21), where we state that the two-particle emission function S_{AB} is (in the case of independent emission) a convolution of two single-particle emission functions. Let us emphasize this complication of the femtoscopic measurement: we are interested in the *single-particle* emission functions, as they directly characterize the source. In contrast, femtoscopy provides information about the *two-particle* (or *relative*) emission functions only. Moreover, the convolution procedure of Eq. (21) is not reversible. It means that, in a strict mathematical sense, one cannot recover the full information about individual single-particle emission functions by measuring only the separation distribution. Nevertheless, in femtoscopic measurements, reasonable additional assumptions can be made and we are able to recover some of the information. In this Appendix we discuss how to extract the single-particle emission function parameters from the measured two-particle ones.

A. Traditional emission function parametrizations

We list here the traditional functional forms of the emission function that are used in femtoscopy and list their parameters. The easiest is the 1D "$R_{\rm inv}$" parametrization:

$$S_{\rm 1D}^{P}(\boldsymbol{r}^*) \equiv \frac{dN}{d^3\boldsymbol{r}} = \exp\left(-\frac{{r^*_{\rm out}}^2 + {r^*_{\rm side}}^2 + {r^*_{\rm long}}^2}{4{R_{\rm inv}}^2}\right),$$
$$S_{\rm 1D}^{P}(r^*) \equiv \frac{dN}{dr^*} = r^{*2}\exp\left(-\frac{r^{*2}}{4{R_{\rm inv}}^2}\right). \tag{A3}$$

Note that the formulas neglect the Δt^* dependence, which is possible thanks to the equal-time approximation in the PRF, allowing one to neglect the Δt^* dependence of $|\Psi|^2$. The change from the 3D variables to the 1D one requires the introduction of the proper Jacobian. Let us also explain the factor of 4 before the "Gaussian σ" $R_{\rm inv}$ instead of the usual 2. It is a particular property of a Gaussian distribution that a convolution of two Gaussians is also a Gaussian, with its σ being the quadratic sum of the σ's of the individual distributions. The $R_{\rm inv}$ parametrization is used for identical particles, for which Eq. (21) can be simplified by noting that both emission functions are the same. If ones assumes that a single-particle emission function is a Gaussian, then the two-particle one is also a Gaussian with σ multiplied by $\sqrt{2}$. Therefore, by fitting the two-particle distribution with the functional form, Eq. (A3), one conveniently obtains the single-particle σ: the $R_{\rm inv}$. Therefore, the $R_{\rm inv}$ "HBT radii" reported by experiments are the single-particle emission function Gaussian widths, where the emission function is assumed to be a 3D Gaussian in the PRF.

A more sophisticated emission function form, used by all RHIC and SPS experiments to report identical pion femtoscopy results, is

$$S_{\rm 3D}^{L}(\boldsymbol{r}) = \exp\left(-\frac{{r_{\rm out}}^2}{4{R^L_{\rm out}}^2} - \frac{{r_{\rm side}}^2}{4{R^L_{\rm side}}^2} - \frac{{r_{\rm long}}^2}{4{R^L_{\rm long}}^2}\right). \tag{A4}$$

We again note the factor of 4 before the σ's, making them the single-particle widths. The important difference is that this emission function has three independent widths, $R^L_{\rm out}$, $R^L_{\rm side}$, and $R^L_{\rm long}$, and they are defined in the LCMS (hence the L superscript), not in the PRF. Note that, unlike in the PRF, we do not use the equal-time approximation in the LCMS. For identical particles this is not a problem: only the Coulomb part of the wave function depends on Δt, but it is factorized out in the usual fitting procedures and replaced with the averaged value. For nonidentical particles one can adopt one of two approaches. One can continue to use Eq. (A5) to be consistent with identical-particle femtoscopy, but in this case the Δt spread will be absorbed into the three spatial radii. Or one can add a fourth component with a time spread to Eq. (A5). Because we aim to compare the results from nonidentical- and identical-particle analysis, and as we are, in any case, only able to recover the dimensionally averaged source size for nonidentical particles, we choose the first solution.

For nonidentical particles we must make one additional modification: the mean emission point should be allowed to differ from 0, at least in the out direction. Moreover, the simple connection between the single- and the two-particle sizes is no longer possible, as the underlying single-particle emission functions are now different:

$$S_{\rm 3D}^{L,N}(\boldsymbol{r}) = \exp\left(-\frac{\left(r_{\rm out} - \mu^L_{\rm out}\right)^2}{2{R^L_{\rm out}}^2} - \frac{{r_{\rm side}}^2}{2{R^L_{\rm side}}^2} - \frac{{r_{\rm long}}^2}{2{R^L_{\rm long}}^2}\right). \tag{A5}$$

We introduced an additional parameter—the mean of the distribution in the out direction $\mu^L_{\rm out}$, and the source sizes are now the two-particle ones.

To facilitate the comparison between 1D and 3D source sizes in the LCMS, we also introduce the emission function with one, directionally averaged, source size in the LCMS, $R^L_{\rm av}$:

$$S_{\rm 1D}^{L,N}(\boldsymbol{r}) = \exp\left(-\frac{\left(r_{\rm out} - \mu^L_{\rm out}\right)^2 + {r_{\rm side}}^2 + {r_{\rm long}}^2}{2{R^L_{\rm av}}^2}\right). \tag{A6}$$

B. Relating one-dimensional and three-dimensional source sizes

Nonidentical-particle femtoscopy has been, so far, limited to measurement of the directionally averaged source size $R^L_{\rm av}$. A question arises: What is the relation between $R^L_{\rm av}$ and three-dimensional source sizes $R_{\rm out}$, $R_{\rm side}$, and $R_{\rm long}$? Let us write explicitly the form of the emission function in the magnitude

of r:

$$S^L_{3D}(\boldsymbol{r}) = \int \exp\left(-\frac{r^2_{out}}{2R^{L\,2}_{out}} - \frac{r^2_{side}}{2R^{L\,2}_{side}} - \frac{r^2_{long}}{2R^{L\,2}_{long}}\right) \times \delta\big(r - \sqrt{r^2_{out} + r^2_{side} + r^2_{long}}\big) dr_{out} dr_{side} dr_{long}. \tag{A7}$$

To find the 1D source size corresponding to the 3D ones, we assume that the preceding distribution can be approximated by

$$S^L_{1D}(r) = r^2 \exp\left(-\frac{r^2}{2R^{L\,2}_{av}}\right). \tag{A8}$$

First, let us note that S^L_{3D} simplifies exactly to S^L_{1D} only in the special case of $R^L_{out} = R^L_{side} = R^L_{long}$, in which case $R^L_{av} = R^L_{out}$. If this condition is not met, the S^L_{3D} is *not* a Gaussian in r, and the exact mathematical relation between the 1D and the 3D sizes does not exist. Nevertheless, for realistic values of radii, S^L_{3D} is not very different from a Gaussian and can be well approximated by S^L_{1D}. One can find an effective approximate relation between R^L_{av} and $(R^L_{out}, R^L_{side}, R^L_{long})$ numerically in the following way. One generates a significant sample of triplets $(r_{out}, r_{side}, r_{long})$, where r_{out} is randomly generated from a Gaussian of width R^L_{out}, r_{side} with width R^L_{side}, etc. Then one constructs a distribution $S(\sqrt{r^2_{out} + r^2_{side} + r^2_{long}})$, to which one fits numerically the functional form, Eq. (A8). The result of the fit, R^L_{av}, is the approximate 1D source size that we seek. We may also want to restrict the fit range to small values of r to minimize the dependence on non-Gaussian features, which will mostly affect the large-r region. We have performed such calculations and concluded that the approximate relation is

$$R^L_{av} = \sqrt{\big(R^{L\,2}_{out} + R^{L\,2}_{side} + R^{L\,2}_{long}\big)/3}. \tag{A9}$$

Note that the pair velocity does not enter into the derivation, so it is equally valid for the LCMS and the PRF.

In addition, in nonidentical-particle femtoscopy one is able to access the first moments of the source distribution. Then S has the general form $S(R^L_{out}, R^L_{side}, R^L_{long}, \mu^L_{out}, \mu^L_{side}, \mu^L_{long})$. Owing to symmetry relations, μ^L_{side} must vanish. For collider experiments with symmetric rapidity acceptance, μ^L_{long} vanishes as well, which leaves one additional parameter, μ^L_{out}. By performing a numerical procedure very similar to the one in the previous paragraph (the only difference being that the r_{out} is now randomly generated from a Gaussian with the mean of μ^L_{out}), we obtained an equivalent approximate effective relation:

$$R^L_{av} = \sqrt{\big(R^{L\,2}_{out} + R^{L\,2}_{side} + R^{L\,2}_{long}\big)/3 + 0.3\mu^{L\,2}_{out}}. \tag{A10}$$

C. Relating single-particle and two-particle sizes

As already mentioned for identical particles, the relation between two-particle and single-particle sizes is a trivial $\sqrt{2}$ factor if the assumption of a Gaussian emission function is made. For nonidentical particle sizes such a simple connection is not possible, and even an approximate one can only be made after certain simplifications are done. Let us assume that the two particle types, A and B, are emitted according to the emission functions S_A and S_B, which are Gaussians. The two-particle emission function is then

$$\begin{aligned} S_{AB}(\boldsymbol{r}) = \int & \exp\left(-\frac{\big(x^A_{out} - \mu^A_{out}\big)^2}{2R^{A\,2}_{out}} - \frac{x^{A\,2}_{side}}{2R^{A\,2}_{side}} - \frac{x^{A\,2}_{long}}{2R^{A\,2}_{long}}\right) \\ & \times \exp\left(-\frac{\big(x^B_{out} - \mu^B_{out}\big)^2}{2R^{B\,2}_{out}} - \frac{x^{B\,2}_{side}}{2R^{B\,2}_{side}} - \frac{x^{B\,2}_{long}}{2R^{B\,2}_{long}}\right) \\ & \times \delta\big(r_{out} - x^A_{out} + x^B_{out}\big) dx^A_{out} dx^B_{out} \\ & \times \delta\big(r_{side} - x^A_{side} + x^B_{side}\big) dx^A_{side} dx^B_{side} \\ & \times \delta\big(r_{long} - x^A_{long} + x^B_{long}\big) dx^A_{long} dx^B_{long}. \end{aligned} \tag{A11}$$

Performing the integration and neglecting the unimportant normalization constants, one obtains

$$\begin{aligned} S_{AB} = & \exp\left(-\frac{\big[r_{out} - \big(\mu^A_{out} - \mu^B_{out}\big)\big]^2}{2\big(R^{A\,2}_{out} + R^{B\,2}_{out}\big)}\right) \\ & \times \exp\left(-\frac{r^2_{side}}{2\big(R^{A\,2}_{side} + R^{B\,2}_{side}\big)}\right) \\ & \times \exp\left(\frac{r^2_{long}}{2\big(R^{A\,2}_{long} + R^{B\,2}_{long}\big)}\right), \end{aligned} \tag{A12}$$

which immediately gives $\mu^{AB}_{out} = \mu^A_{out} - \mu^B_{out}$ and $R^{AB}_x = \sqrt{R^{A\,2}_x + R^{B\,2}_x}$, as expected. Obviously, one cannot recover the two single-particle source sizes from the one two-particle size. However, in this work we have calculated three independent two-particle sizes: for pion-kaon, pion-proton, and kaon-proton systems. Therefore we have a set of three equations, Eqs. (A12), with A and B being π and K in the first one, π and p in the second one, and K and p in the third one, respectively. This set of equations has three unknowns, the single-particle source sizes, R^π, R^K, and R^p, so we can solve it to calculate them.

The procedure has to be carried out in a few steps. We start with the fit values σ_f. From this we calculate the approximate overall averaged source size $R^{\rm av}_f$, following our fit assumptions: $R_{out} = \sigma_f$, $R_{side} = \sigma_f$, and $R_{long} = 1.3\sigma_f$. With these values we write the set of equations for the particle source sizes:

$$\begin{aligned} \sigma^{\pi K}_f &= \sqrt{\sigma^{\pi\,2}_f + \sigma^{K\,2}_f}, \\ \sigma^{\pi p}_f &= \sqrt{\sigma^{\pi\,2}_f + \sigma^{p\,2}_f}, \\ \sigma^{Kp}_f &= \sqrt{\sigma^{K\,2}_f + \sigma^{p}_f 2}, \end{aligned} \tag{A13}$$

and solve it, obtaining

$$\begin{aligned} \sigma^{\pi}_f &= \sqrt{\big(\sigma^{\pi K\,2}_f + \sigma^{\pi p\,2}_f - \sigma^{Kp\,2}_f\big)/2}, \\ \sigma^{K}_f &= \sqrt{\big(\sigma^{\pi K\,2}_f - \sigma^{\pi p\,2}_f + \sigma^{Kp\,2}_f\big)/2}, \\ \sigma^{p}_f &= \sqrt{\big(-\sigma^{\pi K\,2}_f + \sigma^{\pi p\,2}_f + \sigma^{Kp\,2}_f\big)/2}. \end{aligned} \tag{A14}$$

From these fit parameters one then calculates the directionally averaged single-particle radius $R^L_{\rm av}$ with Eq. (A9); σ_f is treated as $R^L_{\rm out}$. These can be compared to the $R^L_{\rm av}$ directionally averaged radius in the LCMS, which can be calculated with Eq. (A9) from the single-particle 3D HBT radii published by the RHIC experiments.

D. Dealing with non-Gaussian source functions

Let us now consider a non-Gaussian source, as it is evident, for example, from this work, that realistic models predict that the emitting source will not have a perfect Gaussian shape. However, the two-particle emission function, defined as a convolution of two single-particle sources, is required to be closer to Gaussian than the single-particle functions. And the single-particle functions themselves, even though non-Gaussian, are not very different: they usually have a large peak and some long-range tails. From this we conclude that even though we know that the two-particle source function is not Gaussian, we may assume that it will have Gaussian-like features: it will have a peak, and the distribution around that peak can be reasonably approximated by a Gaussian. It will also usually have long-range non-Gaussian tails. This means that we can define two variables that can be used as measures of the variance: either the RMS of the distribution or the σ of a Gaussian fit to the peak structure in the emission function. For the study of nonidentical-particle averaged sizes, σ is the proper variable to use. This is because pair wave functions, which are the source of femtoscopic correlation, contain strong structures near 0 r^*, while at large r^* they do not produce any correlation. In contrast, the RMS of the distribution will be very sensitive to the long-range tails, which is undesirable in our case. Therefore we define that the "femtoscopic size" R for a non-Gaussian emission function is simply the σ of a Gaussian fitted to the two-particle emission function near its peak.

E. Obtaining $R_{\rm av}$ from models

In models we know the emission function exactly. Therefore we can infer $R_{\rm av}$ directly from it. We do this numerically, in a manner very similar to the one demonstrated in previous sections. First, we determine the probability distributions for various components of r: $f_o(r_{\rm out})$, $f_s(r_{\rm side})$, and $f_l(r_{\rm long})$. For the THERMINATOR calculation, discussed in this work, we have found that f_o has the form of Eq. (38), f_s is Gaussian, and f_l has the form of Eq. (37). Now we proceed with the generation of triplets, construction of the $S(r)$, and numerical fitting to obtain $R_{\rm av}$. This $R_{\rm av}$ can then be directly compared to the $R_{\rm av}$ obtained from the "experimental" fitting procedure described above.

F. Relations between source sizes in a longitudinally comoving system and the pair rest frame

We can write approximate relations between source sizes in the two reference systems:

$$\begin{aligned} R^*_{\rm out} &= R_{\rm out}\,\langle\gamma_t\rangle\,, \\ R^*_{\rm side} &= R_{\rm side}, \\ R^*_{\rm long} &= R_{\rm long}, \\ \mu_{\rm out} &= \langle\gamma_t\rangle\,\mu^L_{\rm out}. \end{aligned} \tag{A15}$$

Using Eqs. (A9) and and (A10), one can obtain the relations for the averaged 1D radius $R^*_{\rm av}$ as well. One must also independently determine the $\langle\gamma_t\rangle$ for the pair sample used in a given analysis.

[1] G. I. Kopylov and M. I. Podgoretsky, Sov. J. Nucl. Phys. **15**, 219 (1972).
[2] G. I. Kopylov and M. I. Podgoretsky, Sov. J. Nucl. Phys. **18**, 336 (1974).
[3] G. Goldhaber, S. Goldhaber, W.-Y. Lee, and A. Pais, Phys. Rev. **120**, 300 (1960).
[4] R. Hanbury Brown and R. Q. Twiss, Philos. Mag. **45**, 663 (1954).
[5] R. H. Brown and R. Q. Twiss, Nature **177**, 27 (1956).
[6] R. Hanbury Brown and R. Q. Twiss, Nature **178**, 1046 (1956).
[7] R. Lednicky, V. L. Lyuboshits, B. Erazmus, and D. Nouais, Phys. Lett. B **373**, 30 (1996).
[8] S. Voloshin, R. Lednicky, S. Panitkin, and N. Xu, Phys. Rev. Lett. **79**, 4766 (1997).
[9] R. Lednicky, S. Panitkin, and N. Xu, arXiv:nucl-th/0304062 (2003).
[10] R. Lednicky, Phys. Part. Nuclei **40**, 307 (2009).
[11] S. Pratt, Braz. J. Phys. **37**, 871 (2007).
[12] R. Lednicky and V. L. Lyuboshits, Sov. J. Nucl. Phys. **35**, 770 (1982).
[13] D. H. Boal, C. K. Gelbke, and B. K. Jennings, Rev. Mod. Phys. **62**, 553 (1990).
[14] R. Lednicky, J. Phys. G **35**, 125109 (2008).
[15] B. E. A. Erazmus, *Proceedings, CORINNE II, Nantes, France, 6–10 September 1994*, edited by J. Aichelin and D. Ardouin (World Scientific, Singapore, 1994), pp. 116–128; SUBATECH 94-17, Nantes.
[16] R. Kotte *et al.* (FOPI Collaboration), Eur. Phys. J. A **6**, 185 (1999).
[17] D. Gourio *et al.* (INDRA Collaboration), Eur. Phys. J. A **7**, 245 (2000).
[18] R. Ghetti *et al.*, Phys. Rev. Lett. **87**, 102701 (2001).
[19] J. Helgesson, R. Ghetti, and J. Ekman, Phys. Rev. C **73**, 044602 (2006).
[20] J. Adams *et al.* (STAR Collaboration), Nucl. Phys. A **757**, 102 (2005).
[21] K. Adcox *et al.* (PHENIX Collaboration), Nucl. Phys. A **757**, 184 (2005).
[22] U. W. Heinz and P. F. Kolb, arXiv:hep-ph/0204061 (2002).
[23] T. Hirano, Acta Phys. Pol. B **36**, 187 (2005).
[24] M. A. Lisa, S. Pratt, R. Soltz, and U. Wiedemann, Annu. Rev. Nucl. Part. Sci. **55**, 357 (2005).
[25] P. Huovinen and P. V. Ruuskanen, Annu. Rev. Nucl. Part. Sci. **56**, 163 (2006).
[26] W. Broniowski, M. Chojnacki, W. Florkowski, and A. Kisiel, Phys. Rev. Lett. **101**, 022301 (2008).
[27] Y. M. Sinyukov, Acta Phys. Pol. B **37**, 3343 (2006).
[28] Y. M. Sinyukov, A. N. Nazarenko, and I. A. Karpenko, Acta Phys. Pol. B **40**, 1109 (2009).
[29] S. Pratt, Acta Phys. Pol. B **40**, 1249 (2009).

[30] S. Pratt and J. Vredevoogd, Phys. Rev. C **78**, 054906 (2008).
[31] S. A. Voloshin, A. M. Poskanzer, and R. Snellings, arXiv:0809.2949 [nucl-ex] (2008).
[32] P. Sorensen, arXiv:0905.0174 [nucl-ex] (2009).
[33] S. V. Akkelin and Y. M. Sinyukov, Phys. Lett. B **356**, 525 (1995).
[34] C. Gombeaud, T. Lappi, and J.-Y. Ollitrault, arXiv:0901.4908 [nucl-th] (2009).
[35] R. Ledicky, **210**, 0112011 (NA49 note number) (1999).
[36] C. Blume *et al.*, Nucl. Phys. A **715**, 55 (2003).
[37] D. Antonczyk and D. Miskowiec, Braz. J. Phys. **37**, 979 (2007).
[38] D. Miskowiec, arXiv:nucl-ex/9808003 (1998).
[39] J. Adams *et al.* (STAR Collaboration), Phys. Rev. Lett. **91**, 262302 (2003).
[40] P. Chaloupka (STAR Collaboration), arXiv:0705.3480 [nucl-th] (2007).
[41] J. Adams *et al.* (STAR Collaboration), Phys. Rev. C **74**, 064906 (2006).
[42] F. Retiere and M. A. Lisa, Phys. Rev. C **70**, 044907 (2004).
[43] U. W. Heinz and P. F. Kolb, Nucl. Phys. A **702**, 269 (2002).
[44] T. Hirano, K. Morita, S. Muroya, and C. Nonaka, Phys. Rev. C **65**, 061902(R) (2002).
[45] T. Hirano and K. Tsuda, Nucl. Phys. A **715**, 821 (2003).
[46] D. Zschiesche, H. Stöcker, W. Greiner, and S. Schramm, Phys. Rev. C **65**, 064902 (2002).
[47] O. Socolowski Jr., F. Grassi, Y. Hama, and T. Kodama, Phys. Rev. Lett. **93**, 182301 (2004).
[48] A. Kisiel, T. Taluc, W. Broniowski, and W. Florkowski, Comput. Phys. Commun. **174**, 669 (2006).
[49] G. Torrieri *et al.*, Comput. Phys. Commun. **167**, 229 (2005).
[50] A. Kisiel, W. Broniowski, M. Chojnacki, and W. Florkowski, Phys. Rev. C **79**, 014902 (2009).
[51] M. Chojnacki and W. Florkowski, Phys. Rev. C **74**, 034905 (2006).
[52] M. Chojnacki and W. Florkowski, Acta Phys. Pol. B **38**, 3249 (2007).
[53] A. Kisiel, W. Florkowski, W. Broniowski, and J. Pluta, Phys. Rev. C **73**, 064902 (2006).
[54] W. Broniowski, M. Rybczynski, and P. Bozek, arXiv:0710.5731 [nucl-th] (2007).
[55] R. Andrade, F. Grassi, Y. Hama, T. Kodama, and O. Socolowski Jr., Phys. Rev. Lett. **97**, 202302 (2006).
[56] Y. Hama *et al.*, arXiv:0711.4544 [nucl-th] (2007).
[57] D. Kharzeev and M. Nardi, Phys. Lett. B **507**, 121 (2001).
[58] A. Bialas, M. Bleszynski, and W. Czyz, Nucl. Phys. B **111**, 461 (1976).
[59] B. B. Back *et al.* (PHOBOS Collaboration), Phys. Rev. C **65**, 031901 (2002).
[60] B. B. Back *et al.* (PHOBOS Collaboration), Phys. Rev. C **70**, 021902 (2004).
[61] W. M. Yao *et al.* (Particle Data Group Collaboration), J. Phys. G **33**, 1 (2006).
[62] W. Broniowski, P. Bozek, and M. Rybczynski, Phys. Rev. C **76**, 054905 (2007).
[63] Y. Aoki, Z. Fodor, S. D. Katz, and K. K. Szabo, J. High Energy Phys. 01 (2006) 089.
[64] P. Braun-Munzinger, D. Magestro, K. Redlich, and J. Stachel, Phys. Lett. B **518**, 41 (2001).
[65] W. Broniowski and W. Florkowski, Phys. Rev. Lett. **87**, 272302 (2001).
[66] W. Broniowski and W. Florkowski, Phys. Rev. C **65**, 064905 (2002).
[67] J. Rafelski, J. Letessier, and G. Torrieri, Phys. Rev. C **72**, 024905 (2005).
[68] D. Prorok, arXiv:nucl-th/0702042 (2007).
[69] F. Cooper and G. Frye, Phys. Rev. D **10**, 186 (1974).
[70] D. Teaney, J. Lauret, and E. V. Shuryak, Phys. Rev. Lett. **86**, 4783 (2001).
[71] C. Nonaka and S. A. Bass, Phys. Rev. C **75**, 014902 (2007).
[72] T. Hirano, U. W. Heinz, D. Kharzeev, R. Lacey, and Y. Nara, J. Phys. G **34**, S879 (2007).
[73] N. S. Amelin *et al.*, Phys. Rev. C **74**, 064901 (2006).
[74] R. Lednicky, Phys. At. Nucl. **67**, 72 (2004).
[75] R. Lednicky and T. B. Progulova, Z. Phys. C **55**, 295 (1992).
[76] A. Kisiel, Acta Phys. Pol. B **40**, 1155 (2009).
[77] R. Lednicky, Braz. J. Phys. **37**, 939 (2007).
[78] B. Borasoy, R. Nissler, and W. Weise, Eur. Phys. J. A **25**, 79 (2005).
[79] B. E. A. Erazmus, SUBATECH 98-03, Nantes (1998).
[80] R. Lednicky, Acta Phys. Pol. B **40**, 1145 (2009).
[81] P. Danielewicz and S. Pratt, Phys. Rev. C **75**, 034907 (2007).
[82] Z. Chajecki and M. Lisa, Phys. Rev. C **78**, 064903 (2008).
[83] A. Kisiel and D. A. Brown, arXiv:0901.3527 [nucl-ex] (2009).
[84] Y. Sinyukov, R. Lednicky, S. V. Akkelin, J. Pluta, and B. Erazmus, Phys. Lett. B **432**, 248 (1998).
[85] A. Kisiel, Nukleonika **49** (Suppl. 2), S81 (2004).
[86] J. Adams *et al.* (STAR Collaboration), Phys. Rev. C **71**, 044906 (2005).
[87] H. P. Gos, Eur. Phys. J. C **49**, 75 (2007).
[88] S. S. Adler *et al.* (PHENIX Collaboration), Phys. Rev. Lett. **93**, 152302 (2004).
[89] S. S. Adler *et al.* (PHENIX Collaboration), Phys. Rev. Lett. **98**, 132301 (2007).
[90] J. Adams *et al.* (Star Collaboration), Phys. Rev. C **71**, 044906 (2005).
[91] S. Afanasiev (PHENIX Collaboration), arXiv:0903.4863 [nucl-ex] (2009).
[92] A. D. Chacon *et al.*, Phys. Rev. C **43**, 2670 (1991).